Fall 2022

Investigation of Neutrophil-Like HL-60 Cell Migration in a 3D Collagen Matrix

Pouye Sedighian
Claremont Graduate University

Recommended Citation

Sedighian, Pouye. (2022). *Investigation of Neutrophil-Like HL-60 Cell Migration in a 3D Collagen Matrix*. CGU Theses & Dissertations, 467. https://scholarship.claremont.edu/cgu_etd/467.

Investigation of Neutrophil-Like HL-60 Cell Migration in a 3D Collagen Matrix

By

Pouye Sedighian

Claremont Graduate University and California State University-Long Beach

2022

Approval of the Dissertation Committee

This dissertation has been duly read, reviewed, and critiqued by the Committee listed below, which hereby approves the manuscript of Pouye Sedighian as fulfilling the scope and quality requirements for meriting the degree of Doctor of Philosophy in Engineering & Industrial Applied Mathematics.

Perla Ayala, Chair
California State University-Long Beach
Assistant Professor of Biomedical Engineering

Ga-young Kelly Suh
California State University-Long Beach
Assistant Professor of Biomedical Engineering

Claudia Rangel-Escareño
Claremont Graduate University
Adjunct Professor of Mathematics

Ali Nadim
Claremont Graduate University
Professor of Mathematics

Abstract

Investigation of Neutrophil-Like HL-60 Cell Migration in a 3D Collagen Matrix

By

Pouye Sedighian

Claremont Graduate University and California State University-Long Beach: 2022

It is known that cell migration in innate and adaptive immune system plays a fundamental role in human health. Among the immune cells, neutrophils are one of the most essential cells in protecting the body against invading pathogens. In the presence of chemoattractants, these cells are the first responders that start a directed migration toward the injured area. As neutrophils approach the site of infection, they transmigrate to the tissue and follow the chemoattractant concentration gradient to locate and eliminate the invading pathogens. Understanding the patterns and mechanism of neutrophil migration in the presence of chemoattractants could possibly play an important role in discovering new treatments for various immune dysfunction diseases such as sepsis or severe COVID-19.

Here, to study cell migration patterns, we designed a 3D hydrogel model to create a concentration gradient inside a collagen gel that contained neutrophil-like (dHL-60) cells. Our experimental setup and computational analysis allowed us to study the cell migration indicators such as percentage and velocity of motile cells in a 3D environment. Evaluating these cell migration features showed 10 nM Formyl-Met-Leu-Phe (fMLP) was the most suitable initial concentration among 0, 10, and 100 nM fMLP to maximize the cell activity. In addition, as fMLP was invisible under the microscope, we performed experiments with a fluorescent dye that had a similar molecular weight as fMLP to estimate the chemoattractant concentration and its gradient with high

spatiotemporal resolution at any location and time inside the collagen gel. Next, we analyzed the correlation between the cell migration patterns and the chemoattractant concentration and its gradient over time. The results showed that the highest levels of cell motility, measured by a variety of indicators, occurred at moderate fMLP concentrations (5 to 7 nM fMLP) and, counterintuitively, not at the highest concentrations. In summary, the combination of our novel experimental design and computational analysis allowed us to improve on previous studies by correlating the dHL-60 migration indicators to the local chemoattractant concentration at the cell location over time, painting a more complex picture of cell migratory behavior in a 3D environment.

To my best friend, my love, Sahand

And to all the brave Iranian women rising up for freedom

Acknowledgements

I would like to thank my advisor, Perla Ayala, for being supportive and patient with me throughout the past few years. Her patience and positivity especially helped me when many things did not go as planned. Thank you for all the great guidance on my experiments, I did learn a lot. I wish you a healthy and happy life for you and your family.

I would like to thank my amazing lab mate, Daniel Jackson Bursch. He was always very focused, supportive, and on time. Jackson always paid attention to the details and had great ideas of how to make things work better. I could not ask for a better lab mate and friend during this process.

My special gratitude goes to my committee members: Ga-young Kelly Suh for kindly helping me with my qualifying exam and my presentation. Thank you for the great comments on how to present a research project in the best way possible and thank you for being kind. Claudia Rangel-Escareño for teaching amazing topics in computational biology and making me even more excited in statistics and biology. I will never forget your great and engaging classes. Ali Nadim for being a very kind and knowledgeable instructor in the partial differential equations class. I learned a lot and I was able to use what I learned in my research and my job interviews. I am also very grateful for the comments I received from my committee members during my exam.

I would like to thank Dr. Peter Bonate, my manager at Astellas Pharma, for reviewing my thesis, and giving me thoughtful suggestions on my computational analysis. He has been a true example of a kind and caring person. Thank you, Pete, for all the support, I cannot wait to learn more from you at Astellas.

Lastly but not least, I would like to thank my best friend, my beautiful, and very supportive husband, Sahand. He was always there for me when I was down and questioning myself and my research. He helped me lift my project up and change it to something meaningful. I can never thank you enough for your support and kindness. I cannot wait to grow old with you. I am so lucky to have you in my life, I love you so much.

Table of Contents

Chapter 1. Introduction

Neutrophils are one of the most abundant and vital white blood cells in the innate immune system as they maintain and protect the body against bacterial and fungal infections. Upon the maturation of neutrophils in the bone marrow, they are released into the blood vessels to patrol the body against the invading pathogens. Once an injury occurs inside the body, the damaged cells start releasing molecules called chemoattractants to signal the immune cells to migrate toward the injured area. Neutrophils are the first responders to these signaling substances, where they use the chemoattractant concentration gradient to locate the direction of the infected area in a process called chemotaxis (*1-4*). As they approach the source of injury, they squeeze themselves in between endothelial cells to transmigrate to the tissue. Once arrived at the infected site, neutrophils either engulf the bacteria or form sticky webs called neutrophil extracellular traps (NETs) to prevent the pathogens from spreading to other parts of the body (*3*). However, sometimes presence of high amounts of chemoattractants in the body causes neutrophils to damage various organs or even cause death in patients (*1*, *5-7*). For example, sometimes despite the presence of infection, the recruitment of neutrophils toward the site of infection is inadequate compared to a healthy body (*8*). Thus, because of the reduced neutrophil presence at the site of infection, pathogens grow and spread more easily throughout the body (*8*). As a result, damaged cells produce more chemoattractants to recruit the immune cells toward the damaged area, leading to unusual neutrophil behavior such as higher percentage of random migration (chemokinesis) than directed migration (chemotaxis) (*9*) or creation of excessive NETs (*10, 11*), which could contribute to tissue destruction and organ failure (*10-13*). This impaired behavior of immune cells responding to infections is one of the characteristics of sepsis (*8, 9, 13-15*).

In August 1991, sepsis was formally defined by American College of Chest Physicians (ACCP) and Society of Critical Care Medicine (SCCM) consensus conference as an inflammatory response to infection and since then researchers have been coming up with new definitions of sepsis over the years, with the latest definition in 2018 (*16-18*). With every hour passed since sepsis is developed in the patient, the mortality rate increases (*19*). Thus, when sepsis starts developing, the person must go to the hospital right away. But unfortunately, the self-diagnosis of sepsis is a difficult task because the symptoms are similar to COVID-19, flu, or a cold, which include fever, chills, shortness of breath, rapid breathing, pale and discolored skin, and confusion (*14*). Sepsis has negatively impacted the health of millions of people all around the world, causing one out of three deaths in hospitals, making it the leading cause of death in hospitals (*12, 14, 20*).

As mentioned above, neutrophils play an important role in effectively combating pathogens. However, under certain conditions they might contribute to organ damage in patients. Neutrophil migration studies could give us an insight into the complex behavior of neutrophils in fighting pathogens. There is still a lot that is unknown about the chemotaxis of neutrophils. For example, it could be beneficial to study the pattern of cell migration at different chemoattractant concentrations and their gradients in a 3D in-vitro environment over time, or to study the optimum chemoattractant concentration and its gradient to maximize the number of migrating cells and the velocity at which they migrate toward the chemoattractant source in a 3D collagen matrix. A deeper understanding of the pattern and mechanism of neutrophil migration in the presence of chemoattractants could potentially facilitate the development of new treatments for impaired immune cell behavior in various diseases such as sepsis (*4, 5, 10, 16, 21*), Chronic obstructive pulmonary disease (COPD) (*22-25*), or severe COVID-19 (*26-28*) .

Many of the previous studies on cell migration have been restricted to one- or two-dimensional experimental setups while calculating the cell migration indicators such as velocity and speed of motile cells (*29-36*). Although these cell migration experimental setups have been commonly used, they restrict the full 3D cell movements and the physical shape change of neutrophils that occurs in-vivo, making it difficult to translate the findings to cell behavior in the human body.

In addition, previous studies only correlated cell migration indicators (percentage of active cells and their velocities) with the chemoattractant concentration at the source. While these investigations were able to find the optimal initial chemoattractant source concentration required to activate a large percentage of cells, they were unable to correlate the pattern of cell migration to the concentration and its gradient at the exact cell location over time. This limits the amount of information we could gain from observing cell motility over time. Here in our study, we improved the previous designs to quantify the patterns of migrating cells in a high spatiotemporal resolution of concentration and its gradient over time. Below, we present a summary of our experimental and computational study design.

To create a chemoattractant concentration gradient inside the collagen and study the migration of cells in a 3D environment, we designed a 3D chamber using polydimethylsiloxane (PDMS) mold with similar measurements as in previous studies (*37, 38*). Our chamber contained three compartments where the side compartments were designed to hold the chemoattractant and the media and the middle compartment was intended to hold the collagen gel containing cells. Before each experiment, we allowed the chemoattractant in the side compartment to diffuse through the collagen. We then used confocal microscopy to capture the cell movements in a three-dimensional space over time. To analyze the collected data, we created a computational model to automatically detect the cell centers in each time frame and then track the cells using Kalman filtering algorithm over time.

Furthermore, as mentioned above, we were interested in finding a correlation between the patterns of cell movement and our chemoattractant concentration and its gradient over time. To calculate the chemoattractant concentration inside the collagen over time, we had to estimate its diffusion coefficient. But because our selected chemoattractant, Formyl-Met-Leu-Phe (fMLP) was invisible under the microscope, we performed diffusion experiments using a fluorescent dye with a similar molecular weight as fMLP. We estimated the dye diffusion coefficient, hence the fLMP diffusion coefficient, in our collagen matrix using image processing techniques and partial differential equations (PDEs). Calculating the diffusion coefficient of our chemoattractant allowed us to simulate its diffusion throughout the collagen matrix, revealing the concentration and concentration gradient in our proposed model with a much higher in a high spaciotemporal resolution compared to other studies (*30, 35, 39*). Finally, the combination of our novel experimental design and our computational methodology allowed us to study the most suitable initial concentration to activate a high percentage of cells. In addition, we investigated the dependence of cell migration behavior on chemoattractant concentration and its gradient at any location and time inside the collagen matrix.

Each chapter of this thesis explains the details of experimental procedures and data analysis in the study. Here, we present a summary of the contents of each chapter:

Chapter 2 provides an introduction to neutrophils, HL-60 cells, flow cytometry technique, confocal microscopy, and data analysis methods used in the computational model. The chapter first starts by introducing neutrophils, and their important properties when invading pathogens are present in the body. This chapter then explains the difficulties working with neutrophils in in-vitro experiments and it introduces an alternative cell line, HL-60 cells, to study the migration properties of primary neutrophils. Later in the chapter, the flow cytometry technique used in the experiments to confirm the differentiation of HL-60 cells into neutrophil-like cells is discussed. The chapter then introduces confocal microscopy and its applications in 3D imaging of cells. Next, the details of the Otsu's method, an algorithm to estimate the minimum value of a function, is described. This algorithm was used in estimating the diffusion coefficient of the chemoattractant. Finally, a brief description of the Kalman filtering algorithm, which was used in tracking cells inside collagen, is presented.

Chapter 3 first describes the design of our 3D chamber and the measurements used in the experimental setup. It then illustrates the details of preparing the experimental setup using polydimethylsiloxane (PDMS) mold and covers the required steps to prepare mold without any bubbles.

Chapter 4 first describes the details of sample preparation for the fluorescent dye experiments and setup for confocal microscopy. It then explains the details of data analysis in order to compute the dye diffusion coefficient using image processing techniques and partial differential equations. After the estimation of the dye diffusion coefficient, the theoretical results are compared with the experimental data to examine the goodness of the fit in dye concentration profile inside the collagen.

Chapter 5 covers the steps to grow, culture, and differentiate HL-60 cells to neutrophil-like (dHL-60) cells. Next, the process of cell differentiation validation experiments is explained by checking the upregulation of an antigen using flow cytometry. At the end of the chapter, the process of data analysis and results from performing flow cytometry experiments is demonstrated.

Chapter 6 first describes the details of preparing the cells, collagen, and our chemoattractant for confocal microscopy. In section 6.3. , first the steps of noise reduction in images in explained. Next, the image processing techniques applied to detect the cell centers each 3D image is briefly described. These detected centers were then used as the inputs of Kalman filtering algorithm to track each cell over time. The cell tracks allowed us to classify the cell movements and analyze their patterns. In the last subsection of the chapter the results of comparing the cell motilities with different initial chemoattractant concentrations are explained. In addition, the details of more in-depth analysis to understand the patterns of cell migration as a function of chemoattractant and its gradient are described.

Chapter 7 first summarizes the results from the analysis of the collected data at different initial chemoattractant concentrations: 0, 10 and 100 nM fMLP. It then explains our interpretations of our final results and our contributions to the study of cell migration.

Chapter 8 summarizes the entire thesis from the experimental and computational design of our study to reviewing our findings and contribution to the study of cell migration. At the end of the chapter, the limitations of our study and the possible improvements for future studies based on our learnings from our experiments are described.

Chapter 2. Background

2.1. Neutrophils

Neutrophils are the most abundant white blood cells in the innate immune system that are produced and matured in bone marrow. Mature cells are released into the blood vessels to circulate and patrol the body against any invading pathogens. Neutrophils are one of the most essential cells in the immune system as they maintain and protect the body against bacterial and fungal infections. They are the first cells that respond to inflammation and start migrating toward the site of infection to combat with pathogens (*2, 40*). Neutrophils either engulf and digest the bacteria or they form sticky webs to prevent them spreading to other parts of the body (*3, 4*). However, the assistance of neutrophils in killing pathogens can also be damaging and create organ failures and autoimmune diseases (*1, 6, 7, 41*). Hence, understanding the behavior of neutrophils in the presence of infections, play an important role in developing treatments in different infectious and autoimmune diseases (*1, 10*).

The migration of neutrophils starts rapidly upon an occurrence of an injury in the body. This process is started by the damaged cells releasing signaling substances called chemokines, a type of chemoattractant, to direct the neutrophils toward the damaged region. These chemoattractants flow in the bloodstream in hope of finding neutrophils. Once the chemoattractant reaches a neutrophil, it binds to one of the receptors located on the cell membrane. This process leads to chemical reactions inside the cell, polarizing the round shaped cell and causing pseudopods in the front and a knob-like shape called uropod in the back (*42*). Within a few minutes, a large number of neutrophils start their migration. Using the gradient of the released chemokine to find their path toward the infection. As they become closer to the site of injury, they slow down and start sticking and rolling into the walls of blood vessels. Then, they start transmigrating to the tissue by squeezing themselves in-between endothelial cells. Neutrophils continue migrating toward the higher concentration of chemoattractant to find and kill the invading pathogens. This process of directed migration toward chemoattractant gradient is called chemotaxis (*2*, *43*, *44*). In the case of uniform chemoattractant concentration, neutrophils move in random directions. This non-directional movement of the cells is called chemokinesis (*2*).

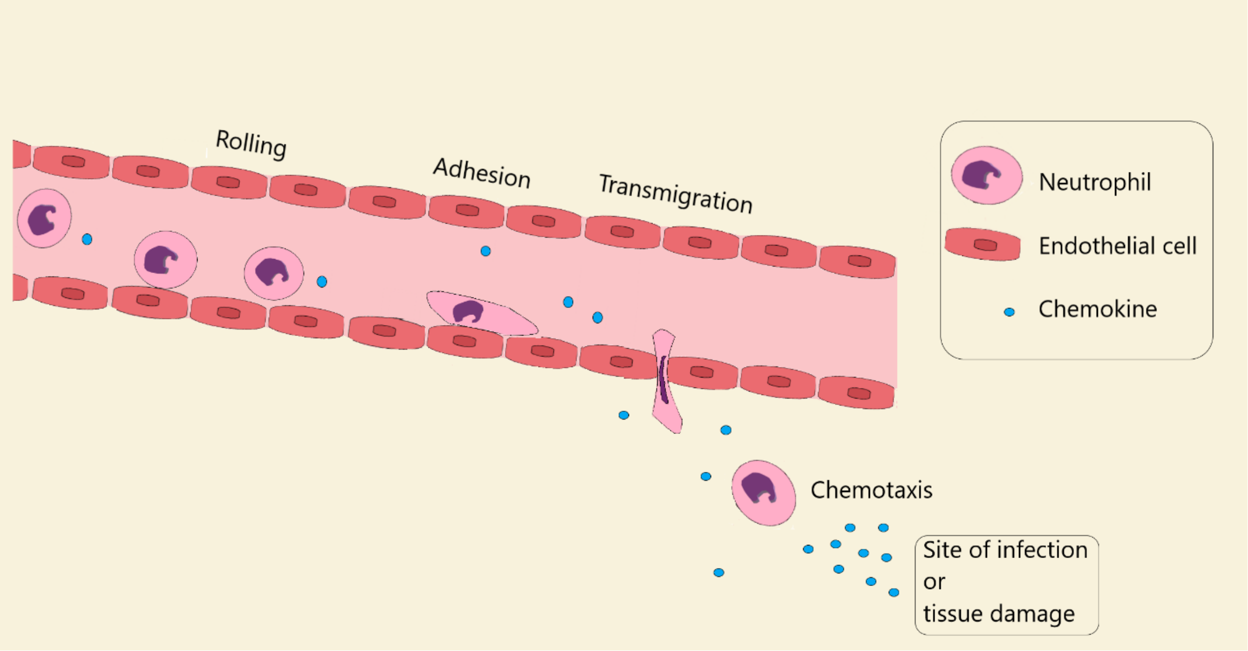

Figure 2.1. The process of directed migration in neutrophils toward the site of infection.

Upon the arrival at the site of injury, early recruited cells also start producing secondary chemoattractants to amplify a more robust chemotaxis toward the pathogens. One of the chemokines that is released in this stage is called leukotriene B4 (LTB_4) which has been shown to enhance the sensitivity of cells toward the primary chemoattractant (*45*). This phase of large recruitment neutrophil is crucial in making sure that cells can kill and prevent the pathogens in overgrowing in the body.

Once neutrophils locate the pathogens, they start engulfing and ingesting the pathogens to clear the area. This process of intracellular killing is called phagocytosis (*10*). In addition to the phagocytosis behavior of cells, neutrophils form a sticky web called neutrophil extracellular traps (NETs) to trap the pathogens and prevent them from spreading to other parts of the body. First, an enzyme called PAD4 inside a cell becomes activated and as a result NETs that are made of neutrophil DNA strands interconnected to antimicrobial peptides and proteins will be created and released (*3, 6*).

To resolve the inflammation caused by an injury, neutrophils are required to clear the area to prevent tissue and organ damage. It has been shown that a large number of cells make U-turns by reversing the polarity inside and enter the blood vessels or the lymphatic system (*46, 47*). The reason of reverse migration of neutrophils is caused by different mechanisms. For example, there might be other chemoattractants present in the vasculature causing the neutrophils to prioritize them over the chemoattractants at the wound. Another possible reason is the release of chemorepellent at the site of infection causing the cells to leave the area. Lastly, the reverse migration of the cells might happen because of the chemoattractant concentration reduction at the area (*1*). While as mentioned above, some cells reverse their migration and enter the vasculature, some act as a sink and upregulate the CC-chemokine receptor 5 (CCR5) to remove the chemokines from the environment to prevent recruiting more neutrophils toward the location. Neutrophils then start shrinking and lose their shape to start the process of death called apoptosis. In this stage, macrophages start phagocytosing the dead neutrophils and clearing the area (*48-50*).

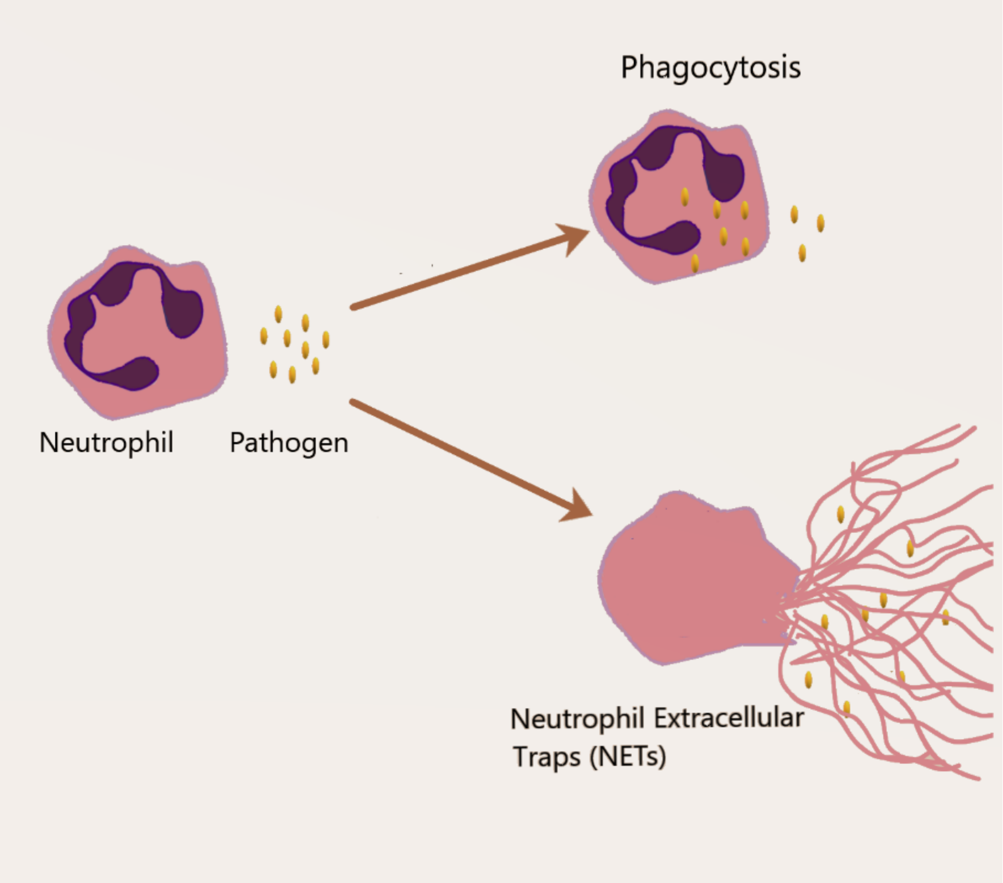

Figure 2.2. Neutrophils combat bacteria in two different ways: 1- They engulf and digest the pathogens to clear the area. This process is called phagocytosis. 2- They release Neutrophil Extracellular Traps (NETs) to trap the pathogens from invading to other parts of the body.

2.2. HL-60 Cells

Neutrophils are the fastest cells arriving at the site of an injury to fight with pathogens. These cells become activated in the presence of chemoattractants and start a directed migration toward the damaged area. Understanding the behavior properties of neutrophils in presence of pathogens guides us in developing treatments for different diseases. Neutrophils are short lived cells, and they cannot be cultured in-vitro. To perform chemotaxis experiments, researchers are required to find various donors, draw blood, and isolate the primary neutrophils from the rest of the cells. After all of these steps, they will only have a limited time to perform the experiment and study the cell migrations. Thus, this makes it difficult to work with neutrophils in in-vitro experiments. As an alternative, many studies use HL-60 cell line to study the mechanical properties of primary neutrophils (*34, 51-53*). HL-60 is a human cell line derived from a 36-year-old woman who suffered from acute promyelocytic leukemia in 1977 (*54-56*). HL-60 cells grow in vitro with simple maintenance, and they double in suspension culture every 36 to 48 hours. Around 5 to 10% of HL-60 cells spontaneously differentiate and represent the same properties of granulocytes such as chemotactic responses to chemokines. But with the help of some reagents, HL-60 cells stop proliferating and start differentiating to various cell lineage such as granulocytes, monocytes, macrophage-like, and eosinophils cells (*55, 57-59*). To promote cell differentiation, 1-1.5% Dimethyl sulfoxide (DMSO) is suggested to be added to the cell growth medium in a period of 5 to 7 days (*53, 60*). As cells start differentiating, they start expressing new receptors such as CD11b, CD68, and CD88 on their membrane (*61, 62*). To confirm the successful differentiation of HL-60 cells, the expression level of the new receptors is tested by flow-cytometry.

2.3. Flow Cytometry

Flow cytometry is a technique that analyzes different cell characteristics such as shape, size, and other properties. This device uses laser beams to excite each cell that is passing through the instrument and collects the light scattered from fluorescence emissions to analyze the cells properties. Flow cytometry also allows us to study the receptor expression on the cell surface by measuring the fluorescence intensity of antibodies bound to those receptors (*63, 64*).

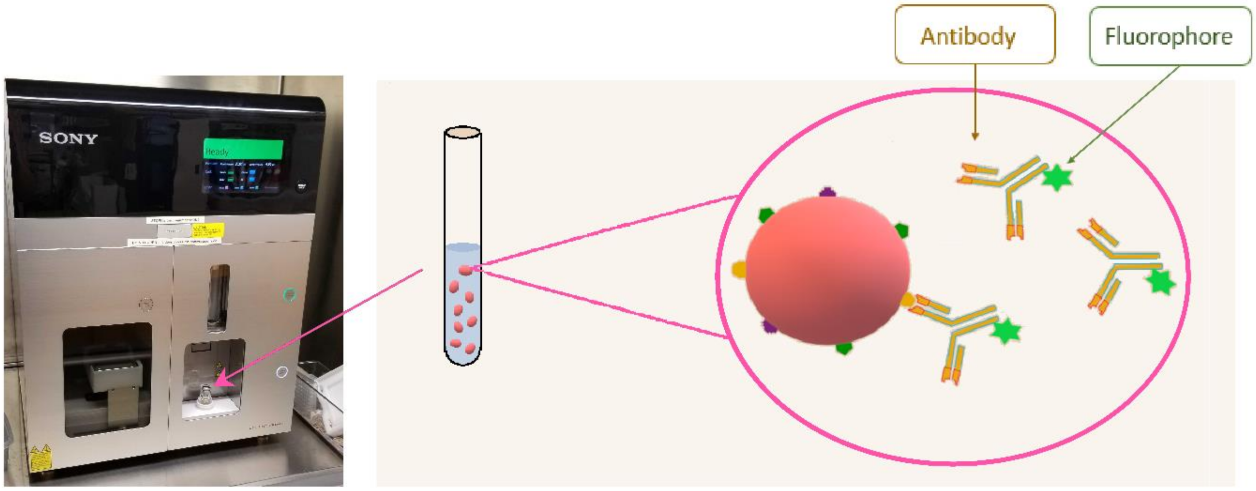

Figure 2.3. Cell sample is labeled with florescent antibodies in the dark for 1 to 2 hours. After the preparation of sample, the tube is placed inside the flow cytometer to analyze the properties of the cells.

To study the properties of the cells, first cells are mixed with FACS buffer (:1X phosphate buffered saline (PBS), fetal bovine serum (FBS), and sodium azide) with the appropriate antibody conjugated to a fluorophore. Once the sample tube is prepared and placed inside the flow cytometer, a nozzle goes into the sample tube and sucks up the cell solution to the device. The cells are then mixed with sheath fluid made of saline solution to go through a narrowing nozzle that allows cells to pass through one by one. Each cell then passes through a laser beam with a correct wavelength of laser light (*65*). Photomultiplier tube (PMT) or photodiodes (APD) collects the scattered emission light from the excited labeled cells with a fluorophore in two different locations. One PMT located along the same axis as the laser beam collects the forward scatter (FSC) light and one located at a 90° angle of the laser light collects the side scatter (SSC) light. FSC provides an estimation of the cell’s size and SSC gives information about the granularity of the cells (*65, 66*). Each detector converts the collected scatter lights into an electrical impulse which is proportional to the amount of fluorophores bound to cells. These electrical pulses are then translated into numerical signals in the computer (*64*). These recordings allow researchers to measure different statistics of their samples.

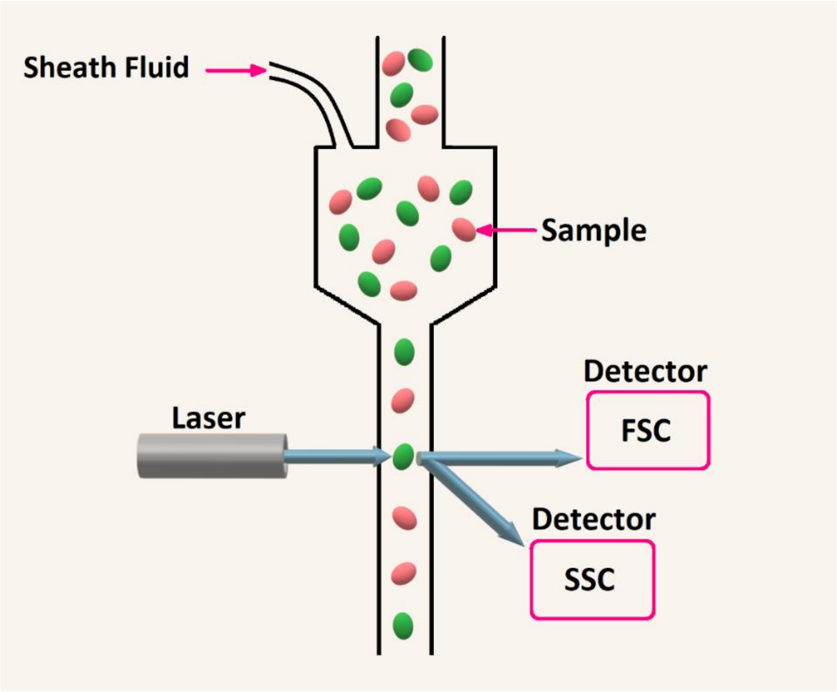

Figure 2.4. Sample cells get mixed with sheath fluid and then line up one by one in a narrow nozzle to go through the laser beam. The emission light is collected using two detectors one placed in the same axis and the other one perpendicular to laser beam.

2.4. Confocal Microscopy

Confocal scanning microscopy is a type of fluorescent microscopy developed by Marvin Minsky in 1955. This type of microscopy captures high resolution images from different z-slices of a specimen and creates 3D images by combining the slices together in a thick samples (*67*). Confocal microscopy uses laser power to excite the fluorophores inside a thin layer of the sample. The laser beam rapidly and sequentially illuminates the area of interest point by point until the whole X-Y plane is covered. The light from the laser excites the electrons within the fluorescent molecules, in turn producing emission light collected through a pinhole (*68*). The pinhole aperture only allows the emission light from the illuminated focal point to pass through. Other lights coming from the outside of the focal point gets rejected by the device. (*69*). Next, a photomultiplier tube amplifies and translate the emission light into a signal which later is converted to a digital image where the pixel values represent light intensities (*67*). The below figure represents a simplified version of a confocal microscopy.

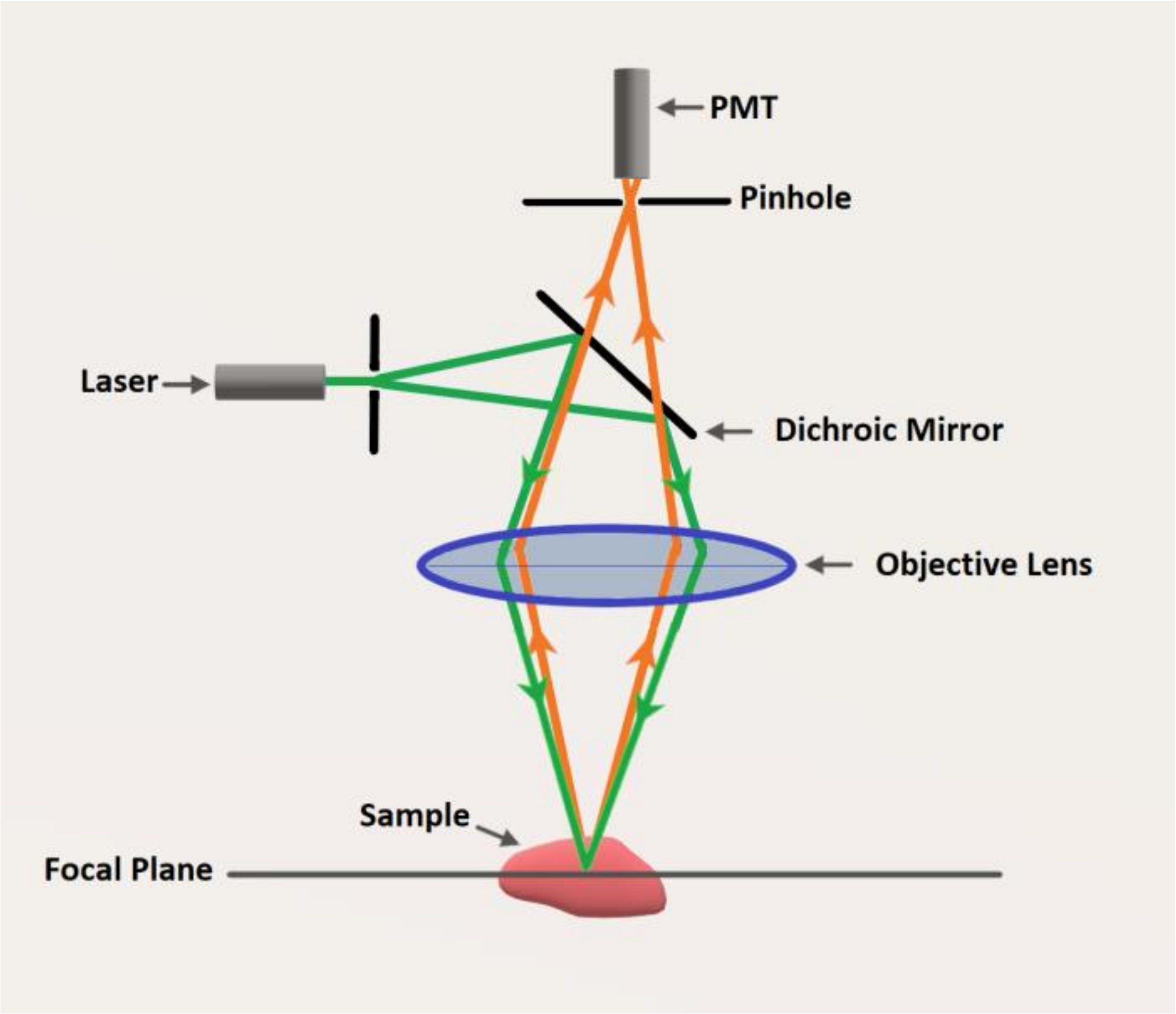

Figure 2.5. In confocal microscopy a laser excites the fluorophores within the sample and then collects the emission light through a pinhole to generate a high-resolution image.

2.5. Data Analysis

2.5.1. Optimization by Nelder-Mead Method

Nelder-Mead Simplex algorithm is a heuristic numerical method that finds the minimum of any given function. In a n-dimensional space, this optimization method defines a simplex around an initial guess using *n+1* test points. The algorithm iteratively keeps replacing the initial guess based on the function values for each test point until the local minima is found or the maximum number of the iterations is met. Nelder-Mead method does not guarantee convergence as it sometimes gets stuck in a flat surface and cannot update the guess to a better answer (*70-72*).

Here is an example of the steps in finding an estimate of the minimum value in a two-dimensional space:

1. **Sort**: Select 3 points (*a, b, c*) to build a simplex and sort them according to their function values in an increasing order: f(*a*) < f(*b*) < f(*c*)
2. **Reflect**: assume f(*c*) gives us the maximum value among all the selected three point. Find the centroid of *ab* and then find reflection of *c* based on the selected centroid and call it *d*. If f(*d*) is smaller than f(*b*) but not f(*a*), accept the new reflected point.

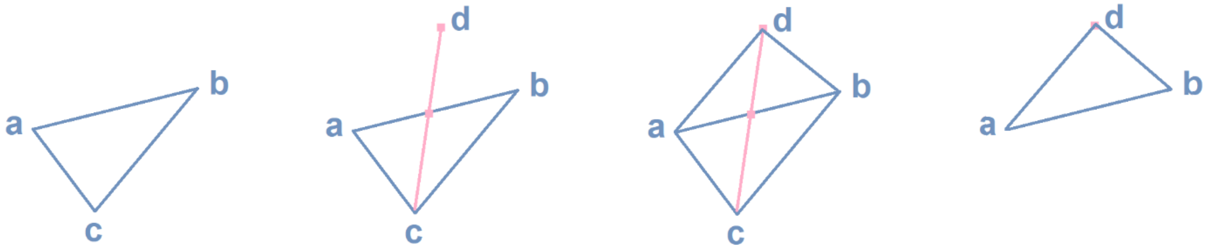

Figure 2.6. Accepting the reflection point (d) as the new estimate of c when f(*d*) < f(*b*) and f(*d*) > f(*a*).

3. **Expand**: If the f(*d*) is better than both f(*a*) and f(*b*), then it means that the selected direction is giving us the best answer. Thus, moving toward that direction even furthermore might help finding the minimum value. As a result, we extend the reflected point toward the same direction by half of the *cd* distance and evaluate the function value of the new point (*e*). If the new expanded point gives us a better answer, we accept it (Figure 2.7). If not, we reject it and keep our reflected point (*d*).

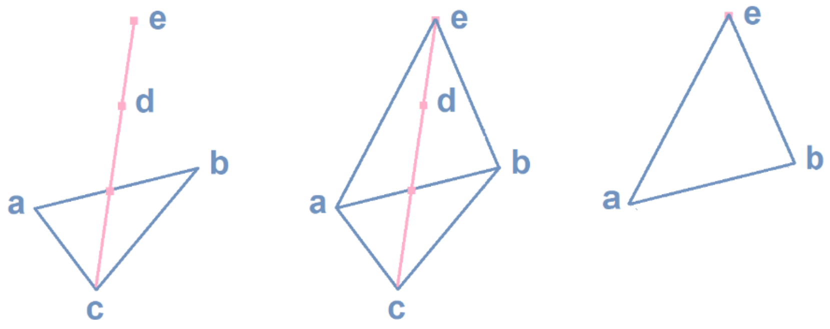

Figure 2.7. Accepting the expansion point (*e*) as the new estimate of *c* when f(*e*) < f(*d*), f(*d*) < f(*a*), and f(*d*) < f(*b*).

4. **Contract**: If the f(*d*) is worse than both f(*a*) and f(*b*), connect *c* to *d* to create a line. Select two points each ¼ distance away from each ending of the created line. Evaluate the value of the function for the two selected points and then select the one with minimum value (Let’s assume it is *f*). If f(*f*) < f(c), accept it and replace *c*, the worst point, with this new point.

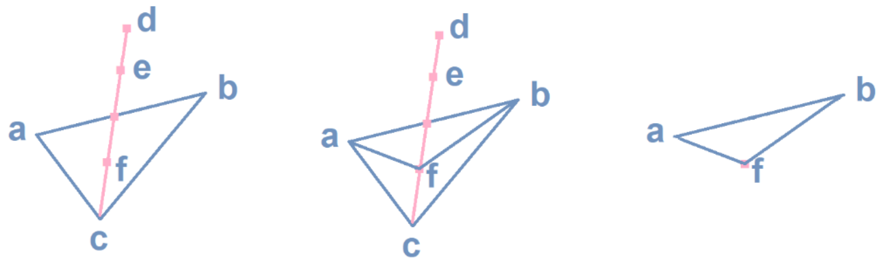

Figure 2.8. Accepting *f* as the new estimate of *c* if f(*f*) < f(*c*).

5. **Shrink**: If none of the above steps are correct, shrink the simplex toward the best performing point by replacing each of the remaining two points, *a* and *b*, with points that are halfway between themselves and the best performing point, a.

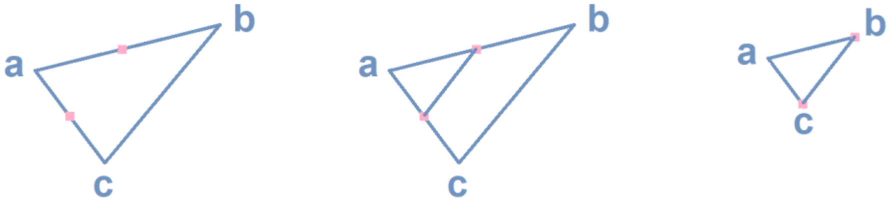

Figure 2.9. Shirking *b* and *c* toward the point with the lowest function value (*a*).

As we continue to repeat the above steps, function values at the *n+1* points become closer and closer to each other. As a result, the standard deviation of the function values at these points becomes closer to zero. Therefore, to estimate whether the convergence has met, we compare the standard deviation with a set threshold. So, when it becomes smaller than our pre-defined threshold we stop the algorithm (*70*, *72*).

2.5.2. Kalman Filter Algorithm

Kalman filtering algorithm is a well-known recursive method that has many applications in different fields such as computer vision (*73-75*). Kalman filter could automatically track objects in a video by predicting their locations in the next frame based on the tracks from the previous frames (*75-77*). Tracking multiple objects in general is a very hard task because occlusions might happen during recording the video. For example, sometimes objects get very close to each other and merge into one object making it difficult to differentiate them from one another for a consecutive number of frames (*76*).

This algorithm requires setting up multiple initial assumptions for the objects to track: First, it assumes objects move with either constant velocity or constant acceleration. Second, it presumes there is Gaussian noise in both the detected centers and the predicted tracks in the model. To start tracking the objects in the first frame, as the algorithm has no information on the patterns of the object movements, it relies on its initial assumptions to predict the location of each object in the second frame. The Kalman filter then selects the closest detected center to its prediction and assigns the labels to those centers. For the rest of the frames, the algorithm uses two main steps to track the objects: 1- At each time frame t_i, the algorithm uses the gained information on the tracks at t_{i-1} to predict the state of an object (its position). 2- In the second step, Kalman filter compares the predicted states with the observed data (centroids) and labels the closest object as its track. It then updates its parameters to minimize the error of its future predictions (*76*). In the incidents where an object disappears, the algorithm keeps its label and its past information of its tracks for a fixed number of the frames. If the object appears again, the algorithm assigns its new location to its tracking label. But if the object is not found during this time, the algorithm deletes its label assuming that it has left the field of view. After all the tracks are assigned, Kalman filter gives new labels to the unassigned detected objects assuming they have just entered the field of view (*75*, *76*).

Chapter 3. Experimental Design

3.1. The 3D Design and Measurements

To study the chemotaxis in a 3D environment, we used similar measurements as (*37, 38*). For each experiment, a 3D chamber was made using a polydimethylsiloxane (PDMS) mold. This chamber had three compartments separated from each other using coverslips. To ensure the exact measurements of the compartments for each experiment, we designed a 3D model using SolidWorks shown in Figure 3.1 and then printed the design by a 3D printer. The 3D prints were carefully washed to remove any residuals left from the machine. For each experiment, a polydimethylsiloxane (PDMS) mold was made using 3D prints.

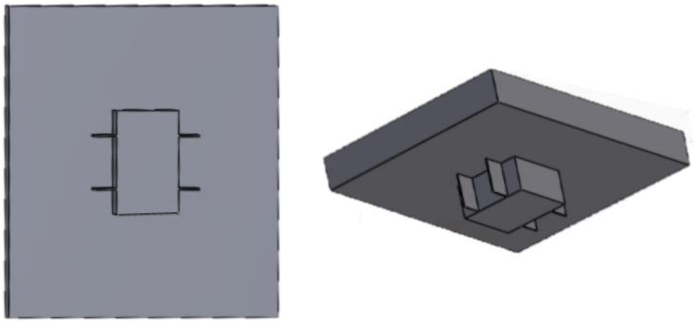

Figure 3.1. Top and side views of the designed 3D model in SolidWorks. We used a 3D printer to print the design and then washed and removed the residuals.

The measurements of the designed 3D chamber are shown in figure 3.2. As mentioned above, the middle compartment contained collagen seeded with cells and the source compartment contained the chemoattractant solution. The sink compartment having the same volume as source held the cell media.

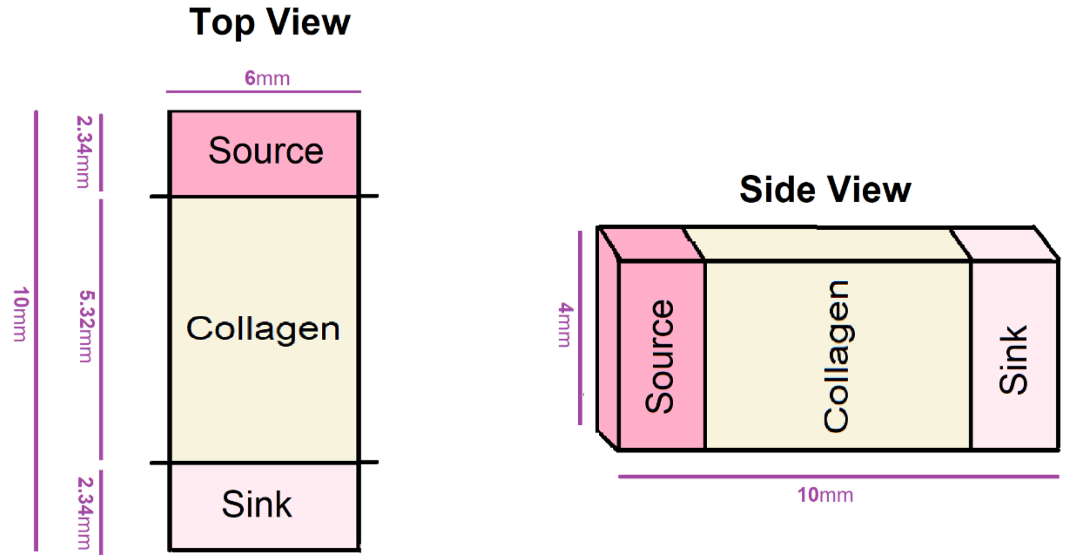

Figure 3.2. Top and side views inside the PDMS mold where the collagen, chemoattractant, and media are added. The total size of the system was 10x6x4 mm where the collagen with length 5.32 mm was located in the middle. The volumes of the side compartments were equal to each other.

3.2. PDMS Mold Preparation

First a ratio of 1:10 curing agent and silicone elastomer base was mixed together in small plate. Then, the mixture was placed in a vacuum for one hour to remove the bubbles trapped inside the solution shown in figure 3.3. This process was very important because bubbles tend to get trapped under 3D prints causing the final PDMS mold to have many tiny holes. Some of these holes could create multiple problems. For example, a hole could cause a diffusion leakage to the collagen and as a result it could reduce the accuracy in our analysis. Another problem would be leakage of the collagen gel to some of the holes before it is completely formed. This results in gels formed with different shapes or volumes. Figure 3.4 shows the results of taking different step to create PDMS molds. As it is presented in the figure, the third strategy worked the best in creating bubble-free molds.

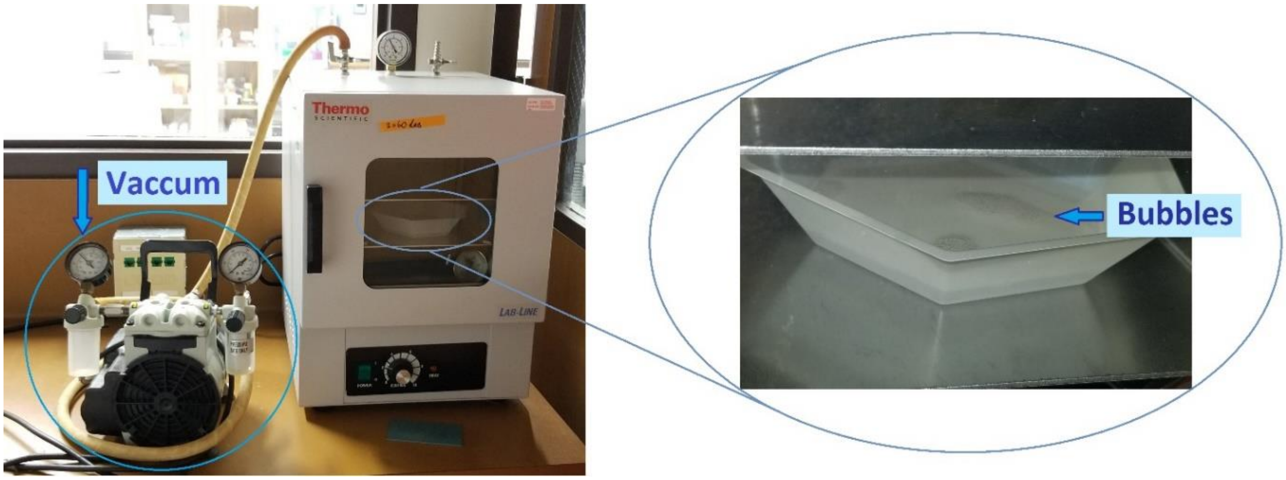

Figure 3.3. The process of vacuuming the PDMS solution to remove the bubbles.

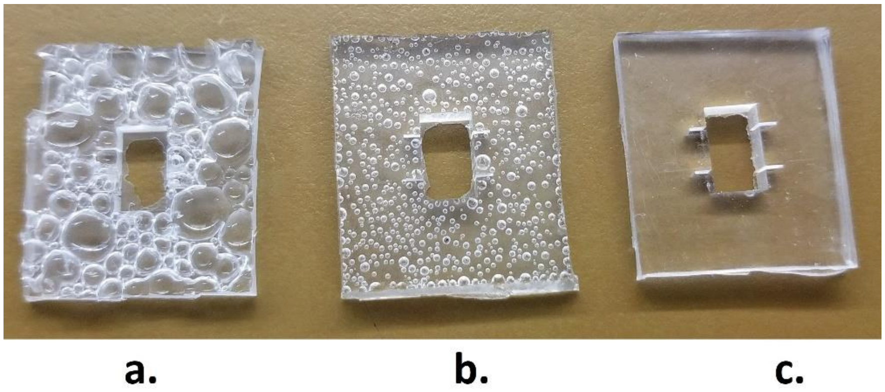

Figure 3.4: **a.** Vacuuming the PDMS solution with the 3D print inside. **b.** Letting the PDMS solution form without any vacuuming. **b.** Placing the PDMS solution on a large plate and vacuuming it for about one hour until all the trapped bubbles are released. And then place the 3D prints into small plates and very slowly pour the vacuumed bubble-free solution. During this stage we made sure to not create any bubbles and if any are created, we took them out using a narrow stick.

After the removal of the bubbles in the solution, the mixture was left at room temperature for 48 hours to form a solid structure. Then, the 3D print mounted to the PDMS mold was carefully removed. The cured PDMS mold was cut on the sides to ensure the proper fit in the final setup. At the end, the mold was washed and cleaned of the small residuals from the cutting. Figure 3.5. shows the steps preparing the cured PDMS molds for the experiments.

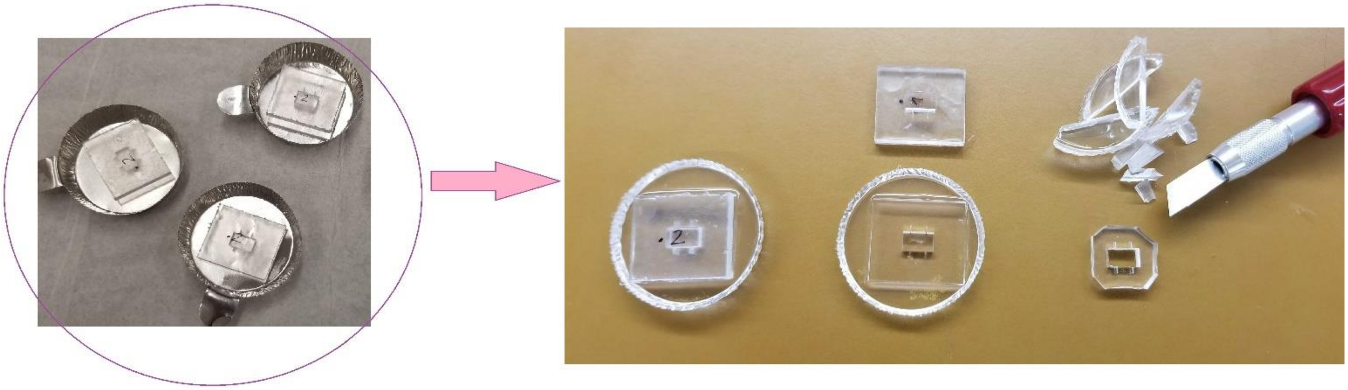

Figure 3.5. The process of removing the 3D prints and cutting the extra edges from the PDMS mold.

3.3. Assembly of The PDMS Mold

To finalize the setup, we needed to secure the bottom of the mold and also separate the compartments from each other. Therefore, silicon glue was used to attach a glass coverslip of size 55x24 mm with the thickness of 0.13 to 0.17 mm to the bottom of the PDMS mold to create a leakage free system. In addition, measured coverslip cuts were inserted into the slits of the PDMS mold to separate the compartments from each other. To cut the coverslips, we used a coverslip from the same batch when securing the bottom of the PDMS mold and created a reference cut rectangle of size 24x9 mm using a caliper and a diamond scribe with a 60-degree angle. We then used our reference cut coverslip to cut the rest of the pieces with the diamond scribe.

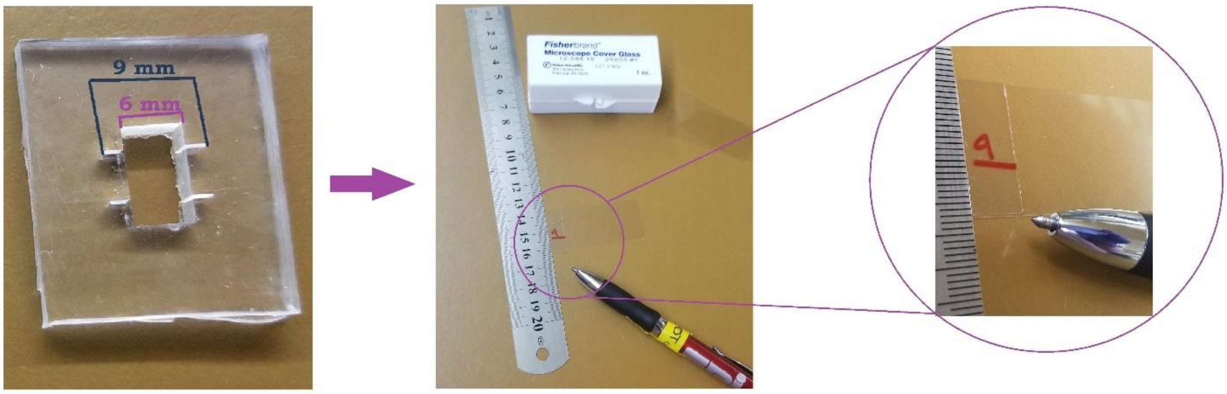

Figure 3.6. The process of cutting the cover glasses into smaller sizes.

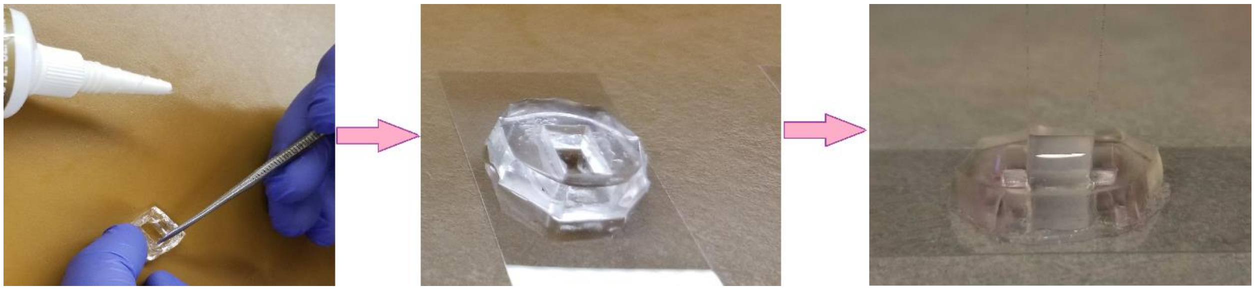

Figure 3.7. To set up the PDMS mold for an experiment, we first attached the PDMS mold to a glass coverslip using a silicon glue. Next, we used small cut coverslips to separate the compartments from each other. We then added the collagen mixture to the middle compartment and let it form in the incubator.

Chapter 4. Fluorescent Dye Experiments

In our study, we designed a 3D system similar to (*38*) that consisted of three compartments allowing us to make collagen in the middle and have chemoattractant on the sides. We used our system to create diffusion from the side compartments to the middle compartment to record the cell migration in the collagen using time lapse imaging in confocal microscopy. One of our questions in our study was finding a correlation between chemotaxis and concentration gradient of our chemoattracts. Therefore, to answer this question, we had to estimate the diffusion coefficient of our chemoattractant. But because the chemoattractants are invisible under the microscope, calculating its concentration gradient at any location and time becomes impossible. As a result, we selected a fluorescent dye, Rhodamine B (RhoB) (ex/em: 553/627) (Sigma-Aldrich, cat. no. 83689), with almost the same molecular weights as fMLP and performed the same diffusion experiments with them. We calculated the diffusion coefficients in our dye experiments and checked the accuracy rate from our theoretical calculations.

Name	**Molecular Weight**
Rhodamine B (RhoB)	479.01
N-Formyl-Met-Leu-Phe (fMLP)	437.55

4.1. Experimental Setup

4.1.1. Sample Preparation

10X PBS-glucose solution: to maintain cell viability, we added glucose to all of our cell experiments. Thus, to stay consistent with our cell experiments, we also added the same amount of glucose to collagen and both side compartments in our dye experiment to create 400 mg/dL glucose. To do that, we mixed 247.4 mg glucose with a 10 mL 10X PBS tube and used that solution for all the following preparations.

Collagen: To prepare a sample for imaging, a prepared PDMS mold was placed in a petri dish inside a biohood with a UV light on for 30 mins. Next, based on the instructions given on the ThermoFisher website, 30 μL 10X PBS-glucose, 5.5 μL 1N NaOH, 220 μL collagen type I, rat tail (ThermoFisher Scientific, cat. no. A1048301), and 44.5 μL cell growth medium (CGM) were mixed together to create a 2.2 mg/mL collagen. Lastly, the final collagen mixture was added to the middle compartment of the mold and then the sample was placed in an incubator for 40 minutes at 37^o C and 5% (vol/vol) CO_2 until a firm gel was formed.

Sink compartment solution: For the side sink mixture, sterile deionized (DI) water was mixed with 10X PBS-glucose and CGM. The concentration of CGM and glucose in both side compartments were exactly the same as the concentrations inside the collagen to create an equilibrium in the system.

Fluorescent dye: To run the dye diffusion experiments, a 5 μM RhoB fluorescent dye was made. To do that, first, a stuck solution with a concentration of 1 mM in 1X PBS was made. Next, we used the equation below to estimate the needed volume from the stuck solution to create 20 mL of our desired concentration, 5 μM, of Rhodamine for our experiments:

$C_sV_s = C_dV_d$

$1000*V_s = 5*20\ \mu L$

$V_s = 100\ \mu L$

Where:

C_s = stuck concentration, C_d = desired concentration, V_s = stuck volume, V_d = desired volume

The calculated V_s was then mixed with a solution of 1X PBS-glucose and 14.8% (2.96 mL) CGM inside.

4.1.2. Confocal Microscopy

After the collagen was made, the stage heater was turned on and placed on the confocal microscopy's stage. A microscope stage heater (AmScope TCS-100 Microscope Temperature Control Stage Slide Warmer) was used to ensure the temperature was maintained at 37 °C in the collagen. After the temperature was reached to our set number, the sample was placed and secured to the stage using a tape preventing any small movements over time. Then, the coverslips in-between the compartments were carefully removed using a tweezer. After the preparation of the setup on the confocal microscopy's stage, the diffusion started by filling both of the side compartments simultaneously by a multichannel pipette. The time of dye insertion was recorded using a timer to be used in the later data analysis. To avoid evaporation of the collagen and dye over time, an aluminum cap was then placed on top of the sample. The stage was then moved in a way to have the edge of the collagen/dye on top of each frame. The time of the moment the Confocal microscopy started to collect the images was recorded to adjust the delay between the insertion of the fluorescent dye and first recorded image.

All the images were recorded using Confocal microscopy model Olympus Fluoview FV1000. We used a 4X air objective (Plan Fluor, NA 0.13, WD 17 mm) and excited the dye with green/yellow diode laser (559 nm) laser. The images of size 512 × 512 pixels (3175 × 3175 μm) were recorded every 30 sec for a duration of 2 hours.

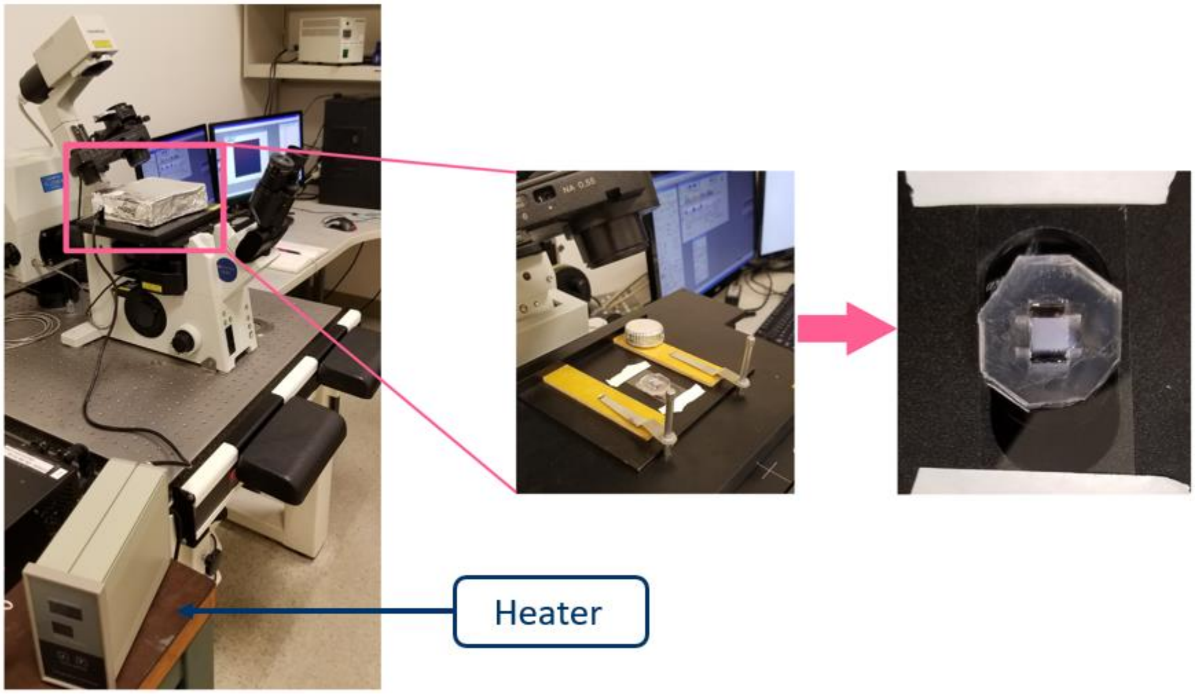

Figure 4.1 An image of a sample when live imaging was done using confocal microscopy. Using tape, the sample was secured to the stage to prevent small movements over time. In addition, an aluminum foil cover was used to prevent the collagen and media from evaporating during the two hours of imaging.

4.2. Data Analysis

After we repeated each fluorescent dye experiments three times, we processed and analyzed all the recorded images in MATLAB (64-bit, version 2019b). Here we assumed the change of the dye concentration profile over time inside the collagen was the same as the change of the pixel values in the collected images. But because for each experiment we had 240 images and the size of each image was 512 x 512 pixels, processing all the pixels was computationally very expensive. As a result, we selected fifteen vertical points and calculated the change of their values over time. To select these points, two important notes needed to be considered:

1. Because there was always a time delay between the beginning of the diffusion and the start time of the first collected image, the pixel values at the top of the image, close to the dye source, were already relatively saturated and did not change much over time. Hence, we focused our analysis on the pixel values that were further away from the diffused parts located on top of the images. To do this, we first found the boundary of the "saturated" region in the first image and selected several equally spaced points below this boundary and monitored the pixel values at these points over time.
2. Due to the inherent uneven brightness in images caused by the optical aberration of the microscope, areas closer to the edges and corners generally appeared darker than the center of the image. We avoided these darker areas by selecting points along the image vertical midline.

To select our 15-pixel points, first all the images were filtered and normalized. Next, the dye diffusion boundary in the first collected image was detected in each experiment followed by the selection of evenly spaced vertical points. Lastly, the change of pixel values in these points was used to estimate the dye diffusion coefficient in the experiments.

4.2.1. Noise Filtering and Normalization

After converting the images into gray scales, we applied the average filtering algorithm to remove the noise and smooth the images. The average filtering technique defines a small moving window that goes through the image pixel by pixel and replaces each pixel value by the average value of the neighboring pixels. This algorithm reduces the intensity variation in the neighboring pixels by smoothing the image. Figure 4.2 shows an example of smoothing a pixel value in an image.

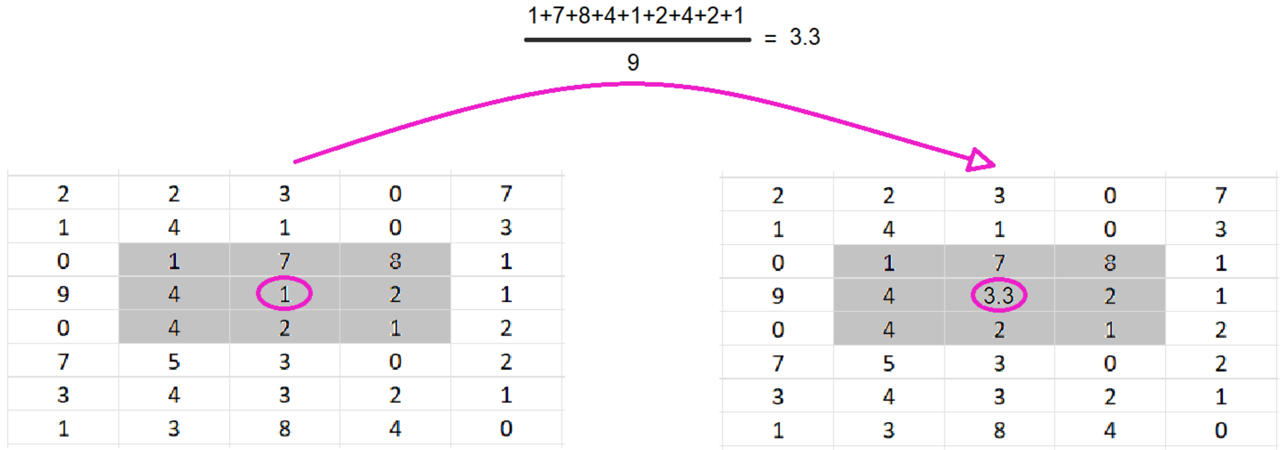

$$\frac{1+7+8+4+1+2+4+2+1}{9} = 3.3$$

2	2	3	0	7
1	4	1	0	3
0	1	7	8	1
9	4	1	2	1
0	4	2	1	2
7	5	3	0	2
3	4	3	2	1
1	3	8	4	0

2	2	3	0	7
1	4	1	0	3
0	1	7	8	1
9	4	3.3	2	1
0	4	2	1	2
7	5	3	0	2
3	4	3	2	1
1	3	8	4	0

Figure 4.2. An example of applying average filtering of size 3x3 to a pixel in an image.

Next, to normalize the data correctly, we needed to divide all the pixel values by the intensity value of the fluorescent dye inside the side compartment. The simplest answer is moving the objective to the side compartment and taking one image from the side compartment with the dye and then calculate the average pixel value in that image as the representation of maximum concentration of the dye at time zero. Then divide all the pixel values by this selected number. This solution had a few issues:

1. Moving the objective to the side compartment and taking an image creates a delay in imaging the diffusion of collagen.
2. In addition, it does not guarantee that the calculated number is correct as the objective has moved and the setup has changed slightly.
3. Lastly but most importantly, the laser intensity needs to be set up to view the diffusion in the collagen. Thus, this requires increasing the laser intensity to see the dye correctly. This might cause saturating the pixel values inside the dye compartment. Therefore, even moving the objective to the side compartment and taking an image, does not help the calculations.

To solve the problem of normalization, different numbers starting from 100 to 500 with an increment of 10 were selected to find an estimate of the average pixel value of the initial concentration of the fluorescent dye. Using each selected number, the whole process of approximating the dye diffusion coefficient was processed and the average error between the estimated theoretical dye concentration profile inside the collagen at different time points was compared with the data from the collected images. Among all the answers, the number that gave the minimum error value was selected in the normalization process. Figure 4.3 is an example of a plot to the sensitivity to normalization in an experiment. Here it is clear that 220 gives the minimum average NRSME among the rest. As a result, this number was selected in the process of normalization.

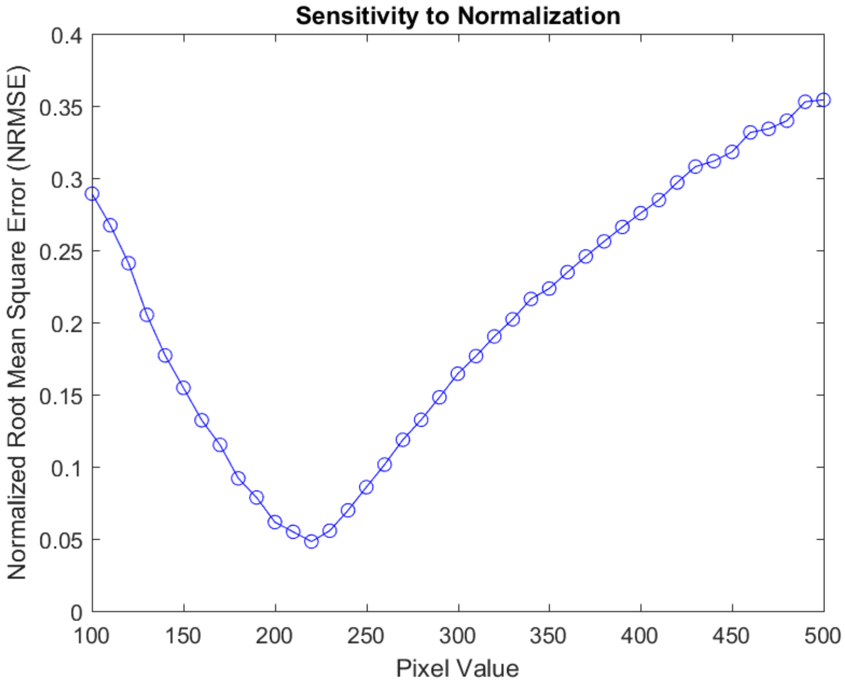

Figure 4.3. Sensitivity to image normalization is measured by calculating the normalized root mean square error (NRMSE) in diffusion profile between the images collected from experiments and theoretical calculations. As shown in this figure, 220 is an optimum value for the normalization step in the experiment. This number varies based on the experiments and the laser power setup when collecting the images.

4.2.2. Boundary Detection

After all the pixel values were normalized, we simply needed to look at their change of value over time to estimate the dye diffusion coefficient. But because analyzing all the pixels was computationally expensive, we only selected 15 equally spaced vertical points under the diffusion boundary in the first collected image and applied them in our data analysis.

To select the vertical points under the diffusion boundary, we first applied a series of following procedures on the first collected frame:

- **Gaussian Filter**: The image was first blurred by Gaussian filter with standard deviation of 5. Similar to average filtering, the Gaussian smoothing kernel blurs the image, but instead of giving the same weight to the neighboring pixels, it employs a normal distribution function to give higher weights to the pixels close to the center than those further away when averaging out the image (*78*). Using this technique, we can remove the gaussian noise in the image.

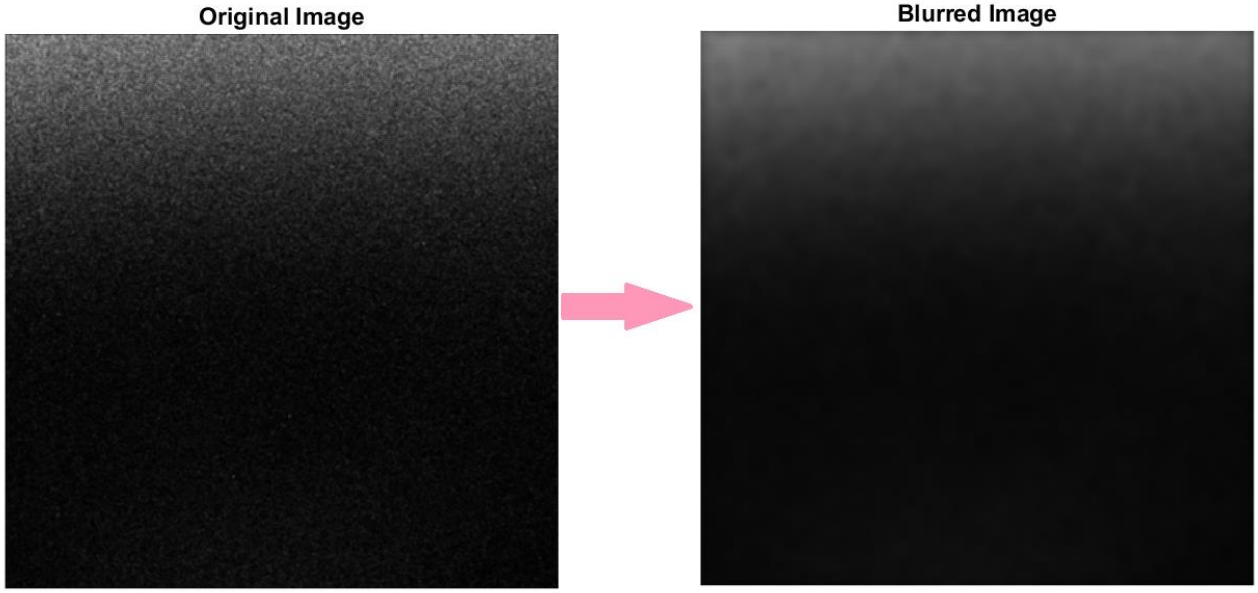

Figure 4.4. The result of applying Gaussian filter to an image to remove the noise.

- **Otsu's Method**: The gray scale image was changed to a binary one to find a better estimation of the dye diffusion boundary. To change the image into a binary one, we need to select a threshold and change all the pixel values above that threshold to one (white) and the ones below to zero (black). To choose an optimal value for the threshold, different algorithms, such as Otsu’s method, can be used. Otsu’s method assumes the image consists of two regions, foreground and background with two different distributions, one belonging to the brighter pixels and one to the darker ones (*79-81*). This algorithm selects a threshold that minimizes intra-class intensity variance between the two peaks of the distributions (*82*).

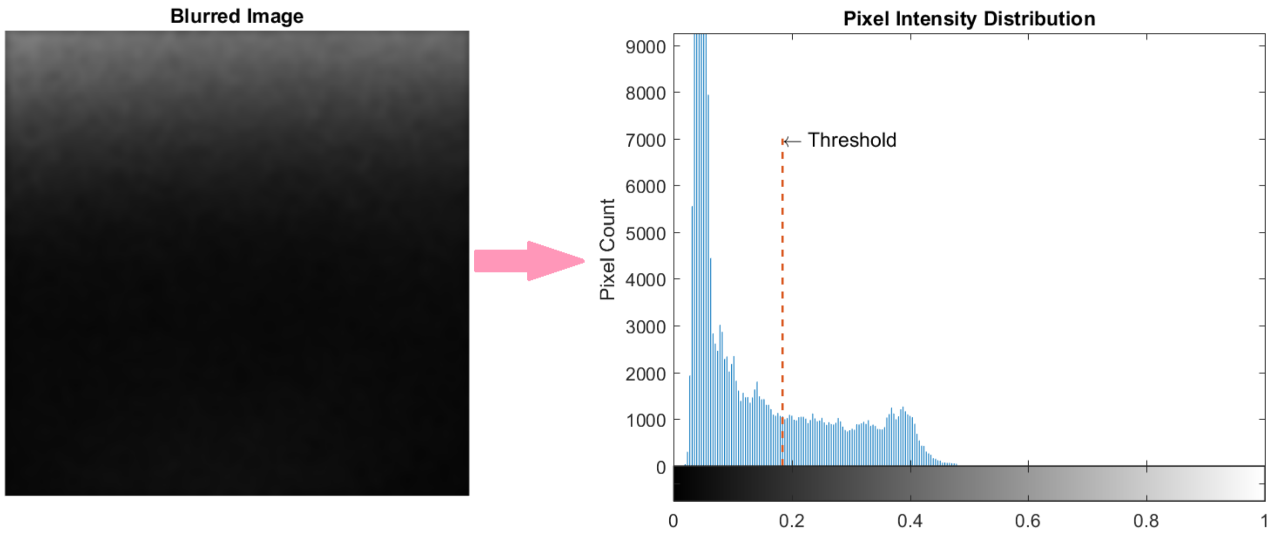

Figure 4.5. Otsu's method is applied to find the best thresholding value in the given image. Please note that the second peak on the right side is much smaller than the one on the left. This is because the first collected image represents the beginning of the dye diffusion. As a result, the total number of brighter pixels become much smaller than the total number of the darker ones.

Boundary Detection: After converting the first frame image for each experiment, the remaining small black holes in the white (diffused) parts were filled with white pixels to create a clear separation between the top (diffused) and bottom (undiffused) of the image (*83*). Next, the diffusion boundary was simply detected by tracing the exterior boundary of the white pixels in each binary image. Finally, we selected 15 evenly spaced vertical points below the detected diffusion boundary and saved their pixel values over time as a representation of the dye concentration inside the collagen. We compared these values with the results from our PDE calculations to analyze the fit between the theory and experiments. The below figure represents an example of the resulting image after each step.

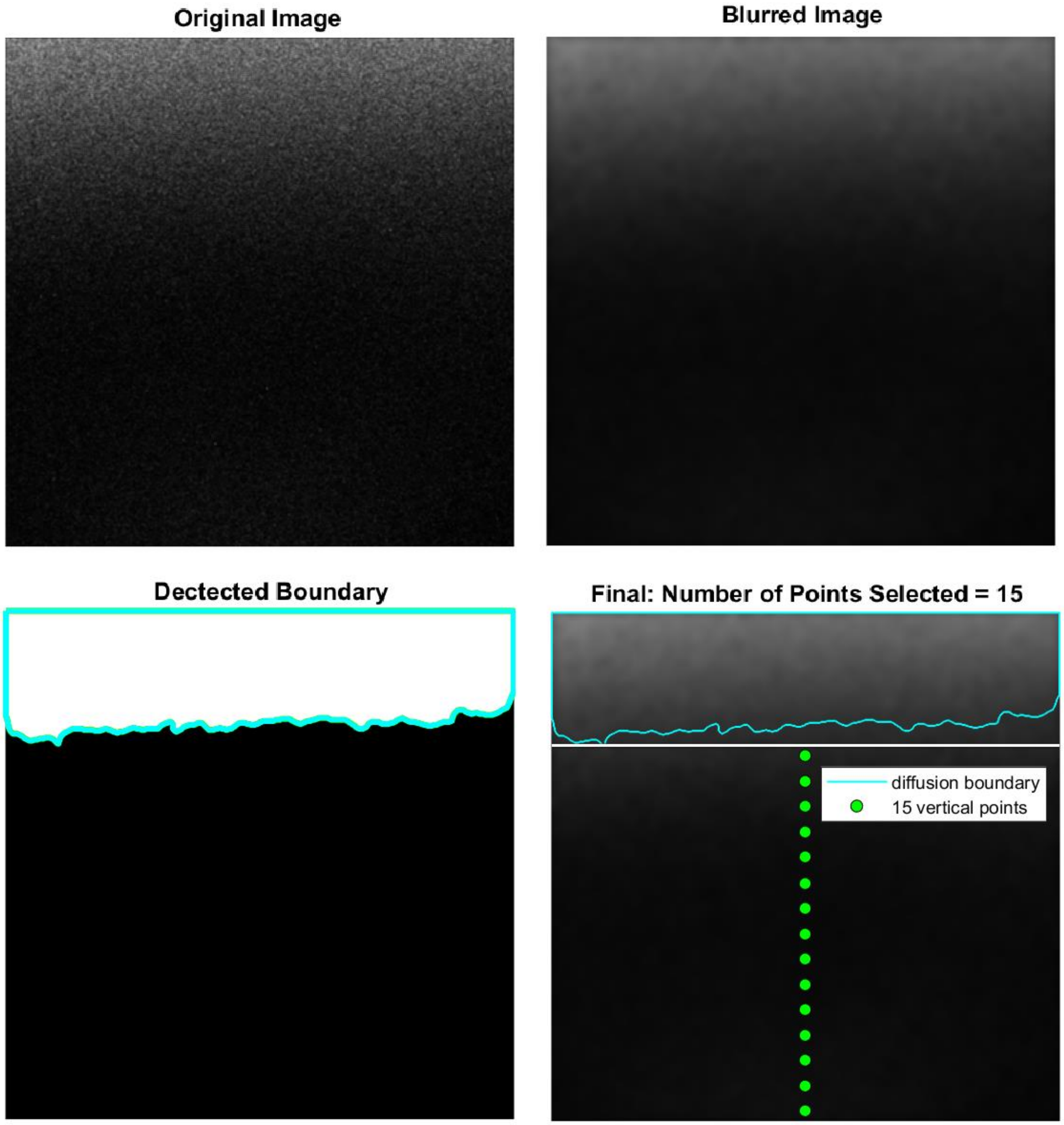

Figure 4.6. As the diffusion already started on top of the first collected image, to select 15 evenly spaced vertical points, we detected the dye diffusion boundary in each experiment. To do that the image was first blurred and changed into binary. Next, the exterior of white pixels was traced to find the diffusion boundary.

- **Smoothing:** In the final stage, robust- Locally Weighted regression Scatterplot Smoother (rlowess) method was applied to smooth the dye concentration in each selected pixel points over time. Robust-lowess is a regression technique that smooths a scatterplot using weighted least squares. This method first takes a subset of the dataset and then locally fits a first-degree polynomial function to the set (*84, 85*). To find the best fit in each selected neighborhood, rlowess algorithm assigns lower weights to the outliers (*85*). The below figure is an example of smoothing the dye concentration at one of the selected vertical points over time.

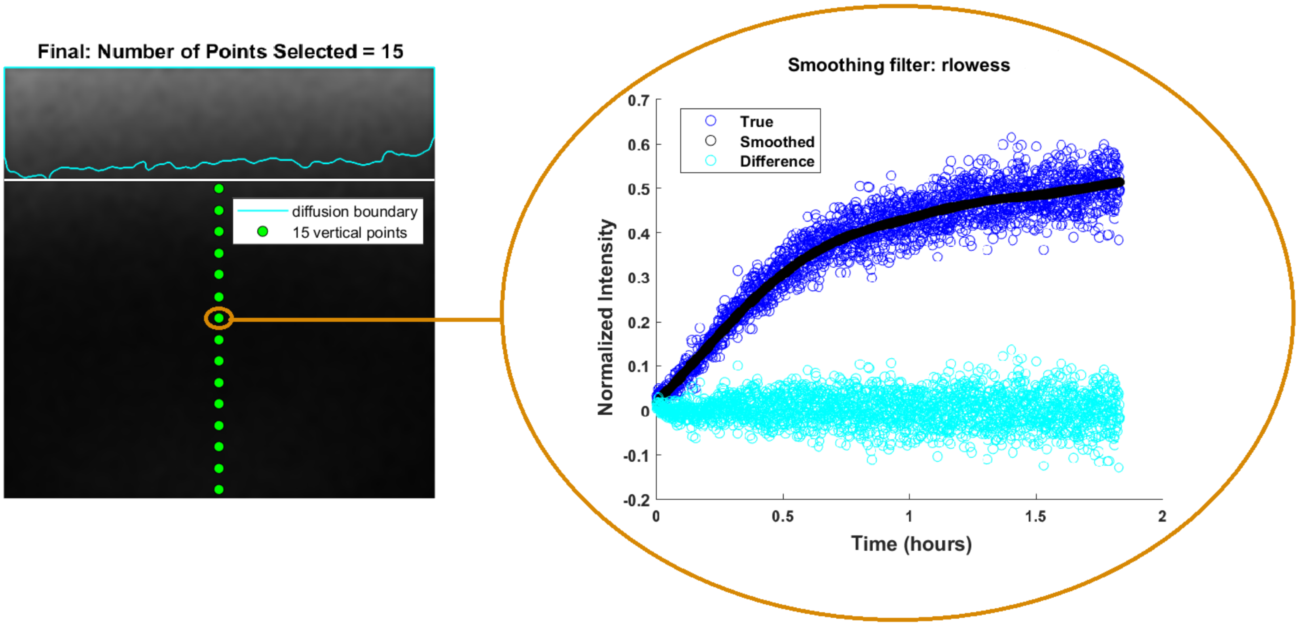

Figure 4.7. Smoothing dye concentration at one point over time.

4.2.3. Diffusion Coefficient Computation

We used Fick's first and second laws to build partial differential equations (PDEs) for each compartment. Because each side compartment was water based, we assumed that the concentration was the same in the entire compartment, but time-variant. To start, we had the below assumptions at $t_0 = 0$:

$$C_{source} = C_0,\ \ C_{sink} = 0,\ \ \vec{C}_{collagen} = [0, 0, 0, \dots], D = D_0$$

Where $C_{source}, C_{sink}, C_{collagen}$ represented the dye concentration in the source, sink, and all the k points along the X axis in the collagen, respectively; C_0 was the dye initial concentration, and D_0 was an initial guess for D.

Next, at each time t_i ($i = 1, \dots, n$) we first updated the concentration values in the collagen using the second Fick's law:

$$(1)\ Fick's\ Second\ Law: \quad \frac{\partial C}{\partial t} = D\frac{\partial^2 C}{\partial x^2} \rightarrow \frac{\Delta C}{\Delta t} = D\frac{\Delta^2 C}{\Delta x^2}$$

To be able to calculate the spatial derivatives at time $t = 0$ and at the collagen boundaries, we had to extend the $\vec{C}_{collagen}$ array by a single value of C_{source} at the start and C_{sink} at the end of the array, increasing the length of $\vec{C}_{collagen}$ from k to k+2 and thus defining the array $\vec{C}_{all} = \left[C_{source}, \vec{C}_{collagen}, C_{sink}\right]$. Assuming $\Delta t = t_{i+1} - t_i$, we can write:

$$(2) \quad \vec{C}^{t_{i+1}}_{collagen} = D\frac{\Delta^2 \vec{C}_{all}}{\Delta x^2}\Delta t + \quad \vec{C}^{t_i}_{collagen}$$

In each time step, after calculating the new $\vec{C}_{collagen}$, we updated the C_{source} and C_{sink} by calculating, using the first Fick's law, the flux out of the source and into the sink based on the first two elements (C_{source} and $\vec{C}_{collagen}$(1)), and the last two elements ($\vec{C}_{collagen}$(k) and C_{sink}) of $\vec{C}_{all}$:

$$(3) \quad Fick's\ First\ Law: \quad J = -D\frac{\partial C}{\partial x} and\ J = \frac{\Delta n}{A\Delta t} \rightarrow \frac{\Delta n}{A\Delta t} = -D\frac{\Delta C}{\Delta x}$$

where Δn is the number of particles entering or leaving the source/sink during the time period Δt, and A is the cross-sectional area of the source/sink. In addition, the particles entering or leaving the source/sink result in a change in the source/sink concentration ($\Delta C_s = C_s^{t_i+1} - C_s^{t_i}$) following the equation $\Delta n = \Delta C_s V_s$, where V_s is the volume of the source/sink. Assuming the source/sink has height h, width w, and length l, its volume can be expressed as $V_s = hwl$. Therefore, equation (3) can be re-written as:

$$(4) \quad \frac{\Delta n}{A\Delta t} = \frac{\Delta C_s V_s}{A\Delta t} = \frac{\Delta C_s hwl}{hw\Delta t} = \frac{\Delta C_s l}{\Delta t} = -D\frac{\Delta C_s^{t_i}}{\Delta x}$$

where $\frac{\Delta C_s^{t_i}}{\Delta x}$ is the spatial concentration gradient at the source/sink at time t_i, with $\Delta C_s^{t_i}$ calculated by:

$$(5) \quad \Delta C_{source}^{t_i} = \vec{C}_{all}^{t_i}(2) - \vec{C}_{all}^{t_i}(1) \quad and \quad \Delta C_{sink}^{t_i} = \vec{C}_{all}^{t_i}(k+2) - \vec{C}_{all}^{t_i}(\mathrm{k}+1)$$

Next, following equation (4) we can find the source/sink concentration at time t_{i+1} by:

$$(6) \quad \Delta C_s = -D\frac{\Delta C_s^{t_i}}{\Delta x} * \frac{\Delta t}{l}$$

$$(7)\quad C_s^{t_i+1} = -D\frac{\Delta C_s^{t_i}}{\Delta x} * \frac{\Delta t}{l} + C_s^{t_i}$$

Once the source/sink concentration was found for the latest time step using equation (7) above, the first and last element (C_{source} and C_{sink}) of $\vec{C}_{all}$ were updated and used in equation (2) to find the $\vec{C}_{collagen}$ of the next time step.

Nelder-Mead Simplex: As both the dye concentration and its diffusion coefficient (D) were unknown in our PDE, we started with an initial guess for D and calculated the dye concentration profile inside the collagen over time. Next, the initial estimate of D was iteratively changed to minimize the sum square error (SSE) between the estimated dye concentration profile inside the collagen using the PDE and our experimental data using the extracted pixel values. This process was done by first defining a function with D as the input and SSE as the output and then estimating its local minima using the Nelder-Mead Simplex method.

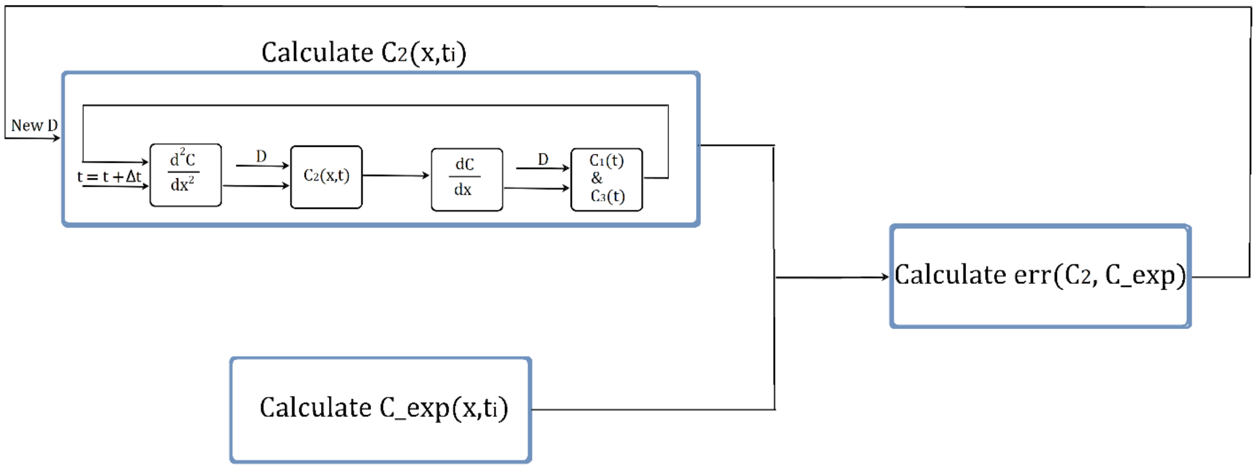

4.3. Results: Estimation of Diffusion Coefficient

In our experiments, because of the small size of the source and the sink compartments, their concentrations were time dependent. As a result, instead of solving our PDE analytically, we solved it numerically. Our assumption for the dye concentration in side compartments was against the hypothesis used in an earlier study (*37*, *38*). Therefore, we calculated the diffusion coefficient based on this earlier study's hypothesis to compare their result with ours. We calculated the normalized root mean square error (NRMSE) of theoretical and experimental diffusion profiles over time for each model. To calculate NRMSE, we first calculated the root of MSE and then divided the result by the difference between the maximum and minimum concentration values of our experimental data. While the NRMSE was very high in the previous method, our results showed that our assumption in time dependency of source and sink concentrations were correct. Thus, the agreement between the theoretical and experimental diffusion profiles in our model showed the suitability of our proposed system to study cell migration in the presence of chemoattractants.

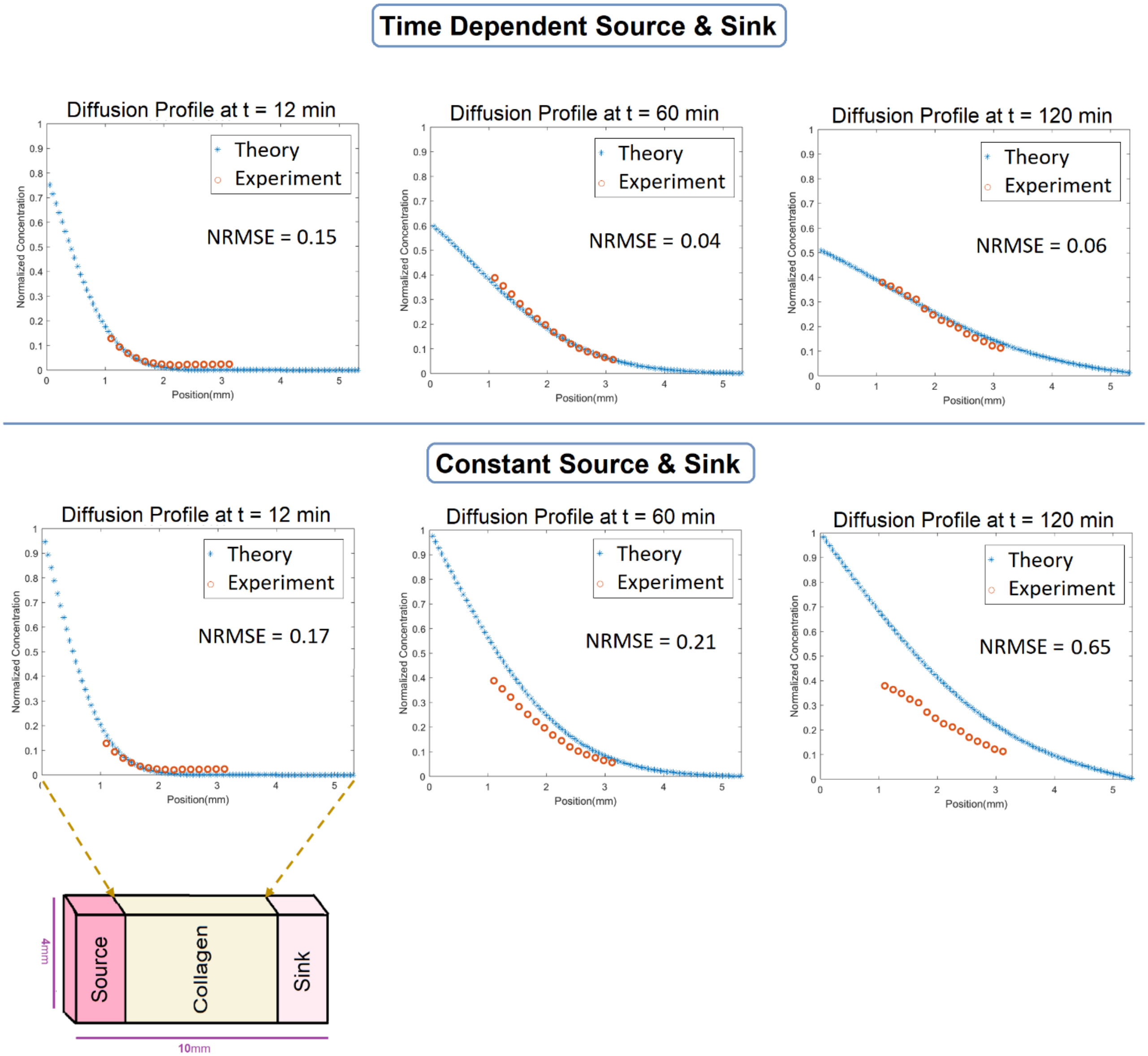

Figure 4.8. Difference between the theoretical and experimental diffusion profiles over time.

Chapter 5. Preparation of Neutrophil-Like Cells

After estimating the chemoattractant diffusion coefficient in dye experiments, we started our cell chemotaxis experiments. We first grew and cultured HL-60 cells and then differentiated them into dHL-60 cells by adding 5% DMSO to the CGM. The cells stayed in the DMSO-CGM solution in the incubator for 6 days. On day 6th, the percentage of differentiation was confirmed using one of the new up-regulating receptors, CD11b, by cell sorter device. Finally, after differentiation validation, we prepared the setup for confocal microscopy.

5.1. HL-60 Cell Culturing and Differentiation

Materials: The human promyelocytic leukemia cell line HL60 were purchased from ATCC (Manassas, VA, cat. no. CCL-240). The cells were cultured in complete growth medium (CGM) consisting of 79% Iscove's Modified Dulbecco's Medium (IMDM) (ATCC, Manassas, VA, cat. no. 30-2005), 20% Fetal Bovine Serum (ATCC, Manassas, VA, cat. no. 30-2020), and 1% of penicillin/streptomycin (ThermoFisher Scientific, cat. no. 15070063).

Culturing: Upon the arrival of the frozen cryovial, the vial was first warmed up in a 37°C water bath for about 2 minutes and then sprayed and cleaned with 70% ethanol. HL-60 cells were transferred to a centrifuge tube that contained 9.0 mL prewarmed CGM and spun at 200 × g for 7 minutes. Supernatant was removed and the cell pellet resuspended in 10 mL CGM. Next, based on the counted number of cells using a hemocytometer, the cell density was reduced to a number between 2×10^5 and 5×10^5 viable cells/mL. The divided cells were transferred to 75-cm^2 Coring cell culture flasks (T75) containing prewarmed incubated CGM, which allowed the pH level to reach an appropriate level for cells to survive and grow.

Every two to three days, 4 to 5 mL fresh CGM was added to each plate until their concentration reached 1×10^6 cells/mL. After the desired density was reached, the cell-media was centrifuged, and the resulting cell pellet diluted in fresh CGU and then divided in new T75 flasks for culturing continuation (*53*).

Freezing: After the first few weeks of cell culturing, we used some of the flasks containing cells and changed their density to 2×10^6 - 5×10^6 cells/mL and froze them. The cells were placed into cryovial of 1mL of CGM with 5% DMSO and left in a –80º freezer for 24 hours. The vials were then transferred into liquid nitrogen for later experiments.

Differentiation: We created DMSO-CGM solution by adding 625 µL (1.25%) DMSO to a 50 mL CGM tube. We transferred the growing HL-60 cells to centrifuge tubes and spun them at 200 × g for 7 minutes. The supernatant was removed, and the pellet was mixed with our DMSO-CGM solution. The cell-media was then transferred to an incubator with 5% CO_2 at 37°C. We added fresh DMSO-CSM solution to each flask every 2-3 days and waited for 6 days to verify the cell differentiation.

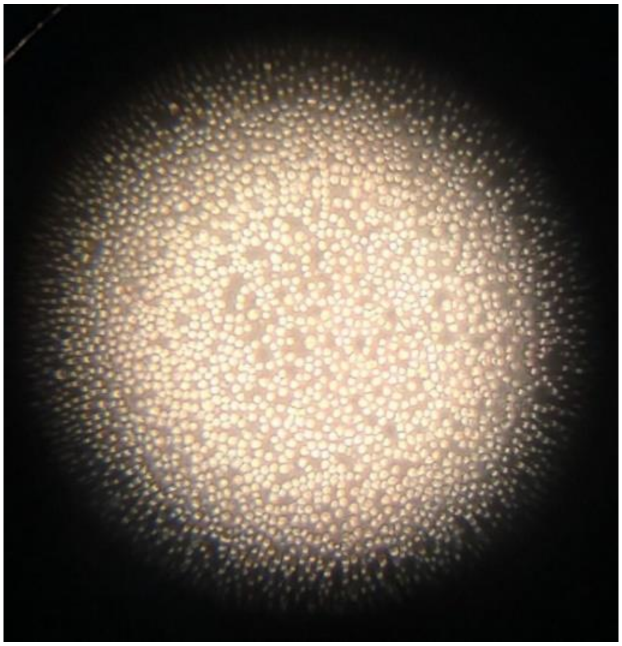

Figure 5.1. An example of HL-60 cells under transmission light microscopy.

5.2. Flow Cytometry Experiments

Previous studies on HL60 cells discuss that HL60 cells start up-regulating different antigens such as CD11b, CD68, and CD88 when they are treated with 1-1.5% DMSO for 5-7 days (*34, 61, 86, 87*). In our study, we compared untreated HL-60 cells with 6-day DMSO treated cells to calculate the percentage of CD11b antigen using Sony Cell Sorter SH800. The results from flow cytometry allowed us to confirm the differentiation of HL-60 cells into, neutrophil-like, dHL-60 cells. As mentioned above, CD11b was chosen as an expression of cell surface differentiation marker in our flow cytometry experiments, and the reason of this selection was because our selected chemoattractant, fMLP, binds to CD11b (*30, 52, 61*). Therefore, confirming the percentage of CD11b surface expression was important in our cell migration experiments.

Materials: the following materials were purchased to perform each experiment: FACS tubes: polypropylene 9×75 tubes (Fisher Scientific, cat. no. 14-956-3B), CD11b Monoclonal Antibody-FITC (ThermoFisher Scientific, cat. no. CD11b01), Mouse IgG1-FITC (ThermoFisher Scientific, cat. no. MG101).

Procedure: the following instructions were then followed to prepare the samples for flow cytometry:

1. Centrifuge 7.5×10^5 viable cells of each group: untreated and 6-day treated HL-60 cells. Resuspend each tube in 500 μL FACS buffer (:1X PBS, 4% FBS, 0.05% sodium azide).
2. Split each tube into three 100 μL in FACS tubes. Note: each cell culture was divided to three groups: control, isotype control, and antibody stained. We used the isotype control samples to determine the level of nonspecific binding in the experiment.
3. Take two of the FACS tubes of each category and mix one with 1 μL anti-CD11b-FITC and one with Isotype-FITC.
4. Incubate all the tubes on ice for 1 hour in dark.
5. Centrifuge each FACS tube at 200 × g for 7 minutes.
6. Remove the FACS buffer and resuspend each tube with 500 μL FACS buffer by vortexing.
7. Repeat the wash by centrifuging each tube at 200 × g for 7 minutes.
8. Resuspend each sample in 300 μL FACS buffer and then keep in the dark until ready for the flow cytometer.

5.2.1. Data Analysis and Results

We repeated each flow cytometry experiment three times and analyzed the collected data using flowJo software. We first separated the live cells from the debris using the gating strategy in the density plot of the side scatter (SSC) versus forward scatter (FSC) profile for each sample (*88*). We then separated the single cells using the forward scatter- height (FSC-H) and forward scatter-area (FSC-A) density plot. Figure 5.2 represents an example of gating strategy separating the live cells from dead cells and subsequently selecting single viable cells in one of the experiments.

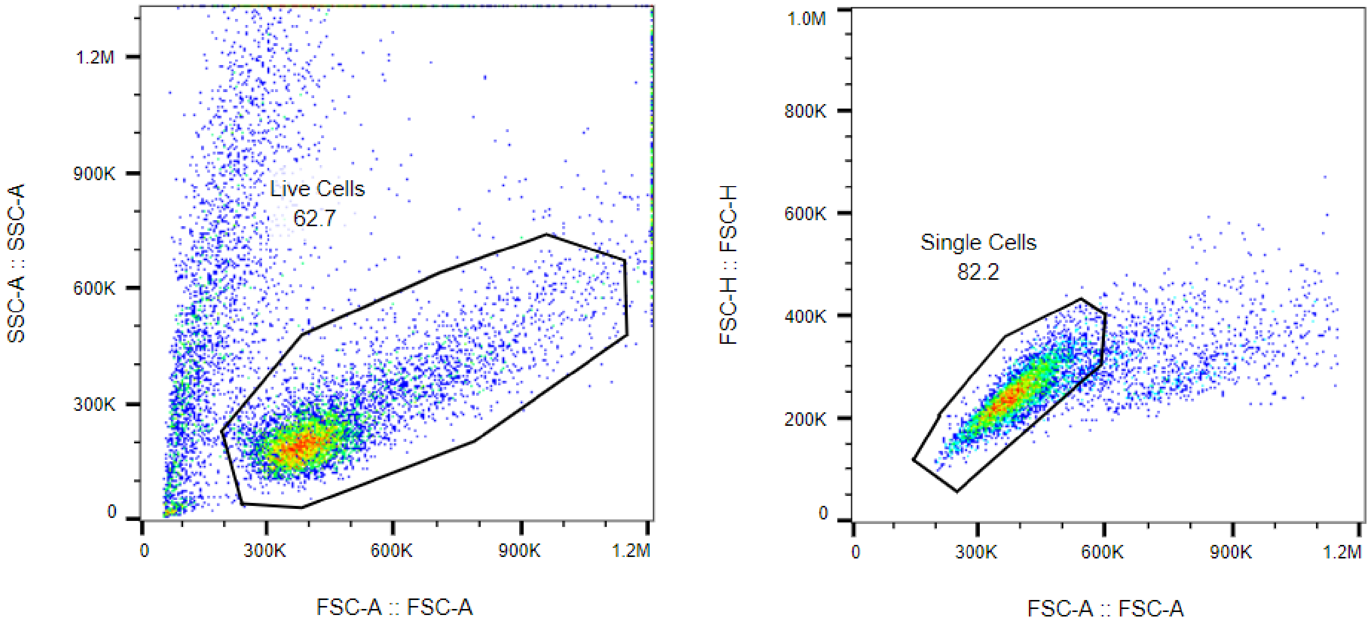

Figure 5.2. The live cells (gated region) were first separated from the dead cells and artifacts in the side scatter (SSC) and forward scatter (FSC) plot. Later, the single cells were separated from the clumps in the forward scatter-height and area plot.

Next, the analysis of CD11b expression surface level for each category, untreated and 6-day treated HL-60 cells, were analyzed for each experiment. Figure 5.3. shows the histogram of florescent intensity values for each category based on the percentage of CD11b expression level. The results from three flow cytometry experiments showed that while the expression rate of CD11b in HL-60 cells was only 26.6 ± 6.01%, CD11b expression rate in dHL-60 cells was 94.47 ± 1.5%. This showed a significant increase in the rate of CD11b expression when treating the cells with DMSO for 6 days, making them an ideal candidate for running the chemotaxis experiments.

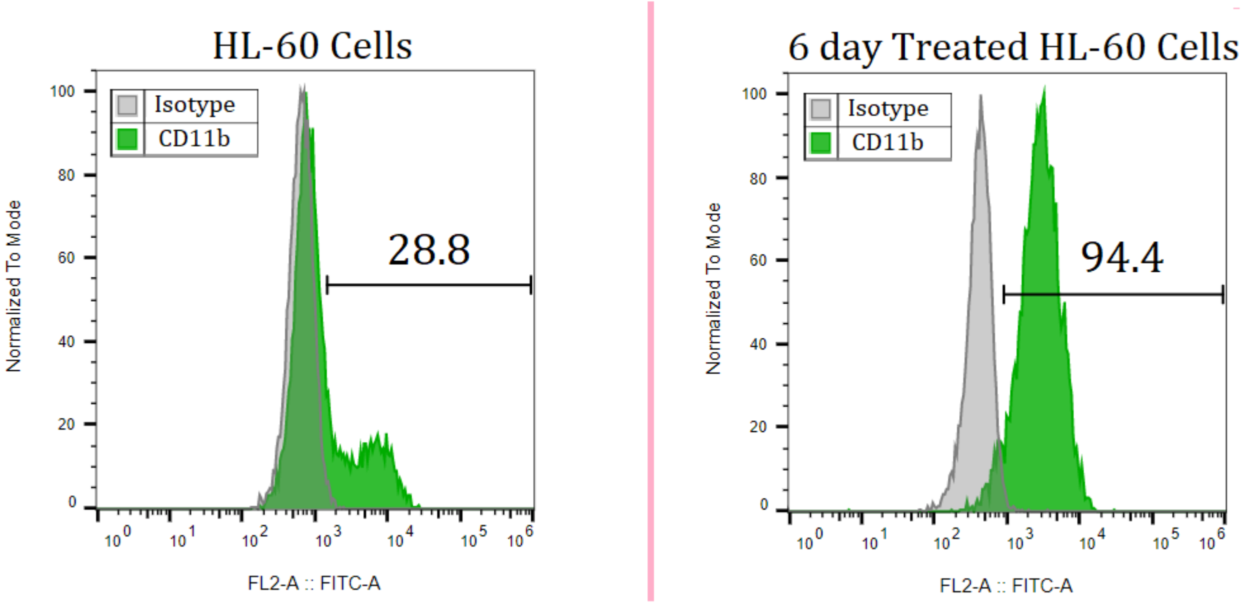

Figure 5.3. An example of the results from flow cytometry detection of the cellular surface differential antigen CD11b for each category.

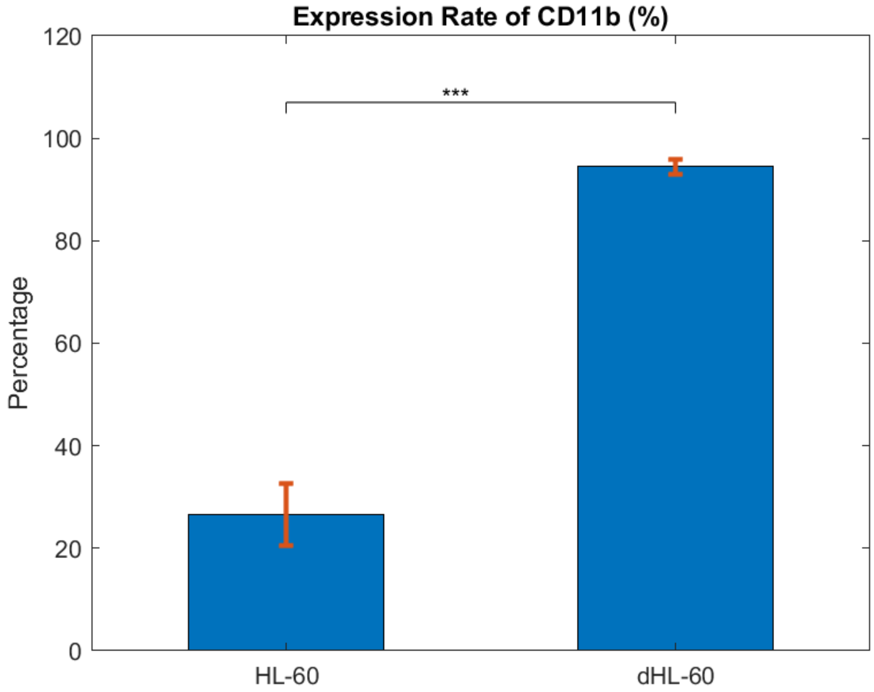

Figure 5.4. Comparison between the percentage of CD11 expression level of HL-60 cells and dHL-60 cells (6-day treated cells with DMSO). The results from a two sample one sided Welch's *t*-test showed the percentages of CD11b expression levels in dHL-60 cells were significantly larger than CD11b expression in HL-60 cells. ($p < 0.001$)

Chapter 6. Cell Migration Experiments

6.1. Sample Preparation

10X PBS-glucose solution: to maintain cell viability, we added glucose when preparing a sample for confocal microscopy. To aim for 400 mg/dL of glucose in the collagen, we added 347.4 mg glucose to a 10 mL 10X PBS. The reason that we added 347.3 mg of glucose was that because we already had 52.61 mg/dL glucose in the collagen that came from 14.8 % CGM used in preparation of the collagen. CGM included 79% IMDM containing 450 mg/dL glucose (52.61 = 0.148 × 0.79 × 450 mg/dL). Finally, to create equilibrium between all the three compartments, we used the PBS-glucose solution instead of PBS for all their solution preparations.

dHL-60 cell staining: CellTracker Deep Red Dye (ex/em: 630⁄650) (ThermoFischer, cat. no. C34565) was used to stain the membrane of the cells. This fluorescent dye was a good candidate for tracking the cellular movements over time since it was nontoxic and kept its fluorescence property for hours.

Before each experiment, we took out a CellTracker vial from a -20°C freezer and DMSO from the refrigerator. We allowed the dye and DMSO to warm up to room temperature. Next, we added 20 µL melted DMSO to our vial to create a 1mM concentration. We diluted 5 µL of the solution with 5 mL of 1X PBS-glucose solution and froze the rest of 15 µl in the freezer. We wrapped the tube that contained the dye solution in a foil and placed it in a water bath. At the same time, we took out the flask containing the cell-media from the incubator and transferred the culture to a conical centrifuge tube. The cells were centrifuged at 200 × g for 7 minutes and resuspended in the pre-warmed dye solution. The cell-dye solution was then incubated in a 25 cm flask at 37°C. After for 30 minutes, we centrifuged stained cells and resuspended the cells in CGM to create around 1.1-

1.4×10^7 viable cells/mL. The cell-media was later used to create the collagen using the same procedure mentioned in chapter 4.

<u>Sink compartment solution</u>: We mixed 100 μL 10X PBS-glucose, 148 μL CGM, and 742 μL DI water to create the solution for the sink solution.

<u>N-Formyl-Met-Leu-Phe (fMLP)</u>: We followed the below procedures to create 10 and 100 nM for the cell migration experiments:

1. Take out the DMSO from the freezer and let it melt to room temperature.
2. Mix 10 mg fMLP with 2.285 mL of DMSO to create a <u>10 mM</u> fMLP solution.
3. Mix 100 μL of the created solution and mix it with 900 μL DMSO to create a <u>1mM</u> fMLP.
4. Next, mix10 μL of the solution in the previous step with 990 μL DI water to make 10 μM fMLP.
5. **<u>To change the concentration to 100 nM</u>**, mix 10 μL of 10 μM fMLP solution with 990 μL PBS-CGM solution (100 μL 10X PBS, 148 μL CGM, 742 μL DI water, 347.6 mg glucose).
6. **<u>To change the concentration to 10 nM</u>**, mix 10 μL of 10 μM fMLP solution from step 4 with 900 μL DI water. This makes 1 μM fMLP solution. Now, mix 10 μL of this solution with 990 μL PBS-CGM solution to create a 10 nM fMLP.

6.2. Confocal Microscopy

The stage setup for confocal microscopy for all the experiments was exactly the same as dye experiments mentioned in chapter 4. After everything was placed correctly, we moved the stage to the edge of the collagen-chemoattractant compartment and found a z-slice of the collagen that contained at cells in our field of view. The moment we started recording, we also stopped the timer from when we poured the chemoattractant. We saved the duration between the insertion of chemoattractant and the start of data collection to estimate the correct concentration profile for our data analysis.

All the images were collected with a 20X air objective (Plan S-Apo, NA 0.75, WD 0.65 mm) using a red diode (635 nm) laser. Every 3 mins, z-stack images of size 512 × 512 pixels (635 × 635 μm) were recorded for a duration of 2 hours. Each recorded z-stack contained 50 slice images with 1.22 μm between each slice.

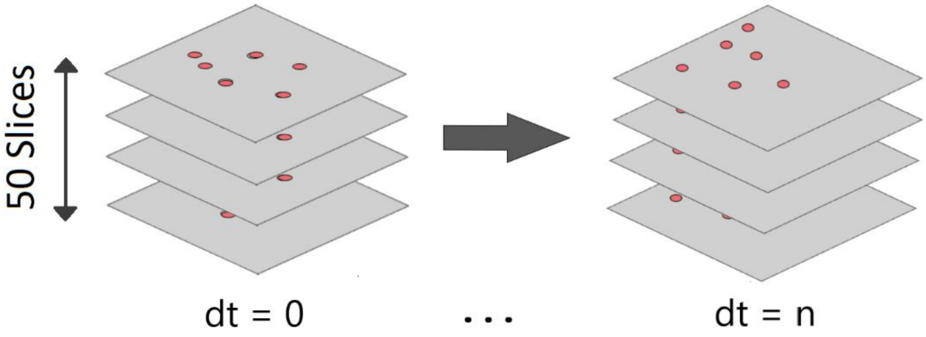

Figure 6.1. Graphical representation of collected z-stack images.

6.3. Data Analysis

As mentioned before, we performed cell migration experiments at three different initial chemoattractant concentrations: 0, 10, 100 nM fMLP. Each experiment was repeated at least three times and the recorded z-stack images were then processed and analyzed in MATLAB (64-bit, version 2019b). To correctly detect and track the movement of the cells, we first removed the shot noises in each image and then normalized the pixel values. Next, we automatically detected the cell centers using Otsu's method. The cell centers were then used to track each cell over time using the Kalman filtering algorithm. Finally, because there was always a drift in the z-dimension, we used the inactive cells that did not move throughout the experiments to calculate the amount of the drift in the z-dimension. We then adjusted the cell movements in the z direction based on our calculations. This adjustment allowed us to have a more accurate data analysis when estimating the cell velocities for each experiment. The details of each taken step in our data analysis is mentioned below.

6.3.1. Noise Filtering and Normalization

We first uploaded the images into MATLAB and then used the pixel values in the red channel to convert them into two dimensional gray images. We then removed the shot noises by applying the median filtering technique. This method is one of the blurring techniques in computer vision that replaces each pixel value with the median value in a 3-by-3 matrix around the point. This pixel median value replacement reduces the intensity variation in the input picture. The below figure is an example of removing the shot noises in a Z-stack of an experiment using median filtering. To create an easier visualization, all the Z-stack images at time zero are added together to create one single image.

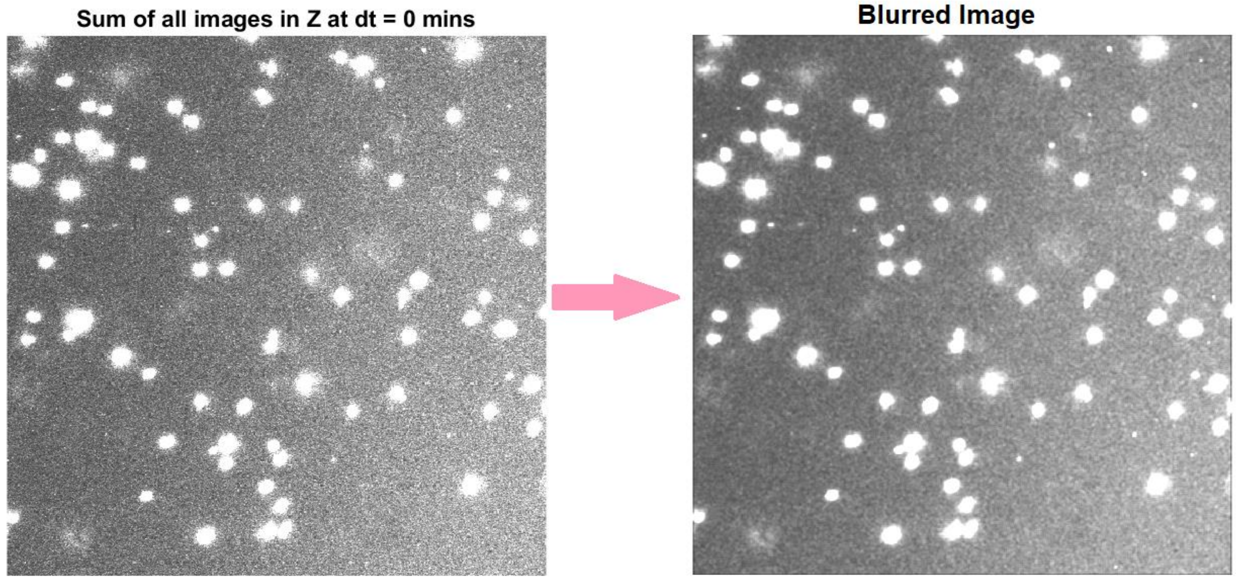

Figure 6.2. An example of removing the salt pepper noise in an image using the median filtering.

Finally, all the pixel values in each image were normalized to a range of 0-1 by dividing each pixel by the maximum intensity value.

6.3.2. Cell Detection and Center Calculation

The images were first changed into binary ones separating the cells from the background. The binary images were the results of changing the pixel values above an Otsu’s threshold to 1 and the rest to 0. Otsu’s algorithm separates the pixels into two foreground and background categories. It looks at the histogram counts of the pixel values and automatically picks a point that separates the two peaks representing the foreground and background in the image. Using this selected point, we convert a gray scale image into a binary one by changing pixel values above this point to 1 and the ones below to 0. Here, we used one third of the calculated threshold to include the darker boundary parts of the cells creating the actual shape of the cells.

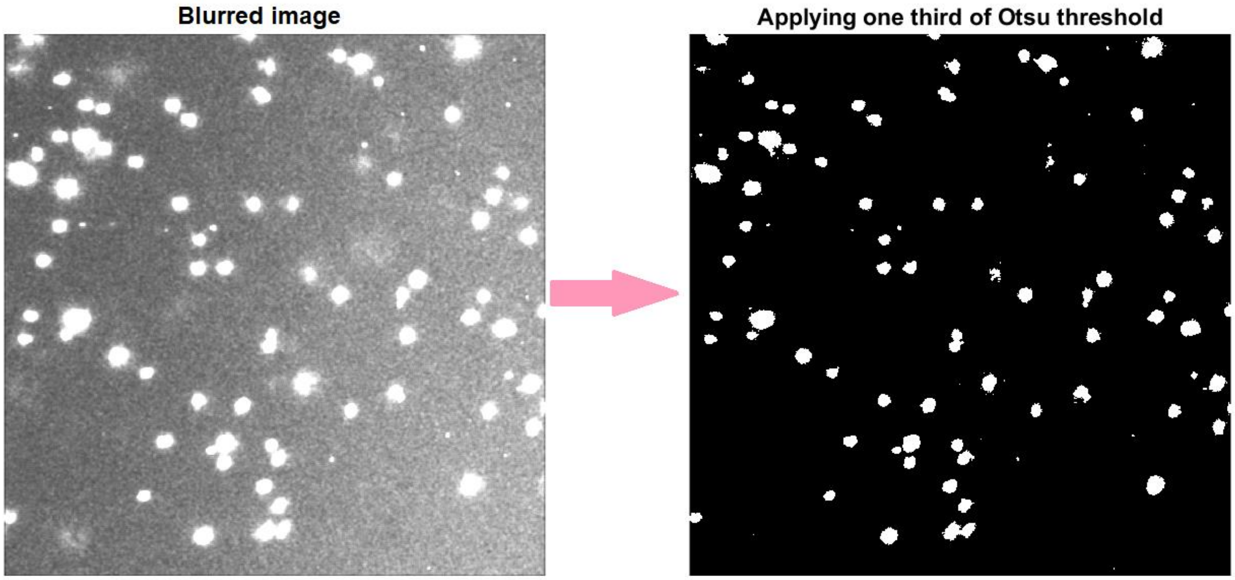

Figure 6.3. The result of applying one third of Otsu's threshold in a blurred image.

In the resulting binary images, the small bright spots from artifacts or particles from dead cells were eliminated. As the size of these artifacts were very small, first using the union-find algorithm the connected components were detected and then their total number of the white pixels were counted. Figure 6.4. shows an example of a binary image containing multiple connected components (cells). The union-find algorithm first assumes each white pixel is a separate cell by giving each pixel a unique label. It then starts scanning the image column wise and forming a union for any neighboring white pixels by connecting their unique labels into one common label.

In this example, the selected sub-image contains two separate cells, and the surroundings of the cells are just black pixels. Performing the union-find algorithm on this sub-image results in finding two labels (cells).

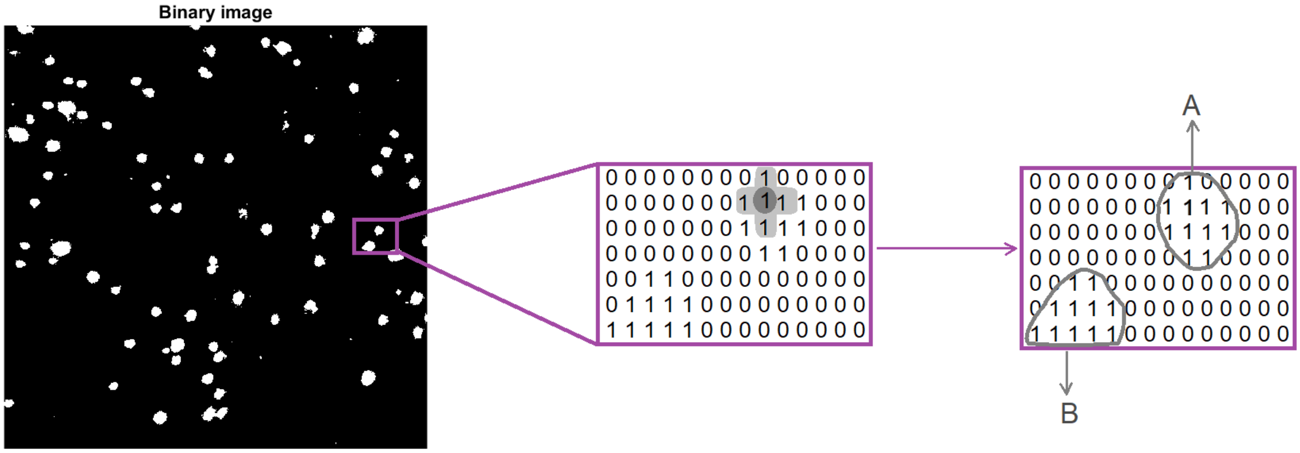

```
0 0 0 0 0 0 0 0 1 0 0 0 0 0
0 0 0 0 0 0 0 1 1 1 1 0 0 0
0 0 0 0 0 0 0 1 1 1 1 0 0 0
0 0 0 0 0 0 0 0 1 1 0 0 0 0
0 0 1 1 0 0 0 0 0 0 0 0 0 0
0 1 1 1 1 0 0 0 0 0 0 0 0 0
1 1 1 1 1 0 0 0 0 0 0 0 0 0
```

```
0 0 0 0 0 0 0 0 1 0 0 0 0 0
0 0 0 0 0 0 0 1 1 1 1 0 0 0
0 0 0 0 0 0 0 1 1 1 1 0 0 0
0 0 0 0 0 0 0 0 1 1 0 0 0 0
0 0 1 1 0 0 0 0 0 0 0 0 0 0
0 1 1 1 1 0 0 0 0 0 0 0 0 0
1 1 1 1 1 0 0 0 0 0 0 0 0 0
```

Figure 6.4. An example of finding the connected components in a binary image.

After applying the union-find method, the total number of white pixels in each connected component was counted and the ones that had less than 30 pixels were labeled as artifacts and removed from the images. Figure 6.5 represents an example before and after the removal of small white spots in a binary image.

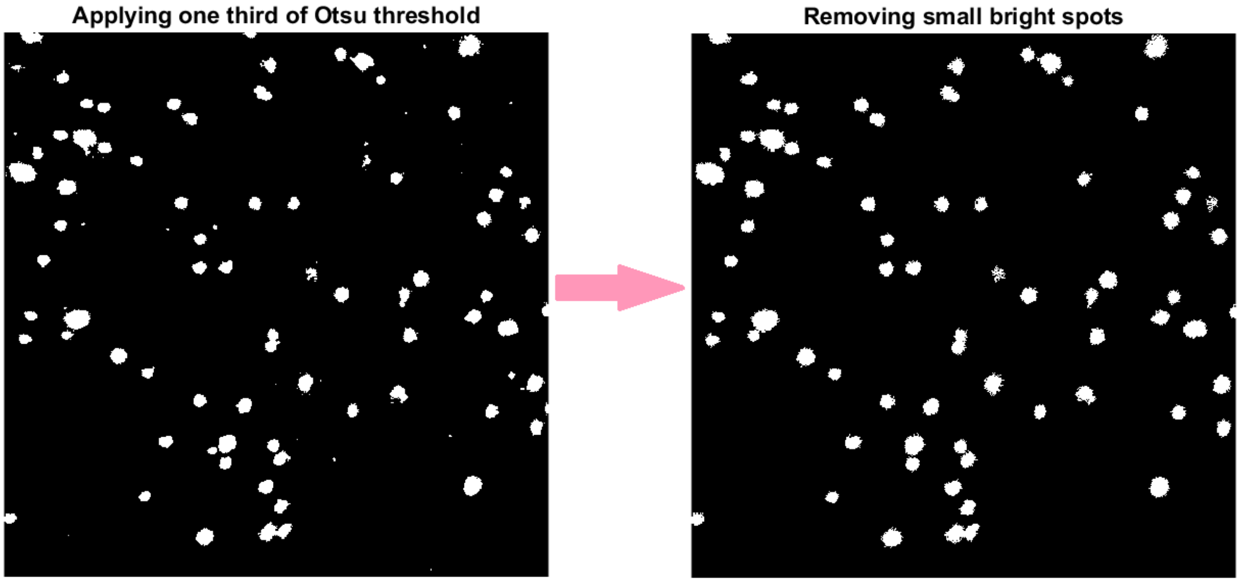

Figure 6.5. An example of removing small bright spots that had less than 30 pixels in the binary image.

The binary images belonging to the same z-stacks were then placed into 3D tensors to build the 3D shapes of the cells. The surrounding white pixels around each pixel was searched to detect the connected components in the 3D space. Figure 6.6 is the graphical representation of the searched directions to create the cell shapes. After the detection of cell shapes, their centroids were calculated by taking the average value of the range of their pixel locations. These centroids were then used as the inputs of the cell tracker algorithm to trace the cell movements over time.

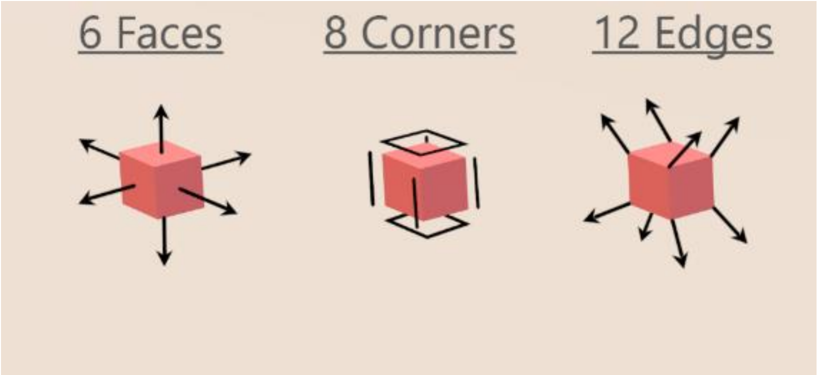

Figure 6.6. Any two pixels that are neighbors in one the three cases: faces, corners, or edges are considered part of the same cell.

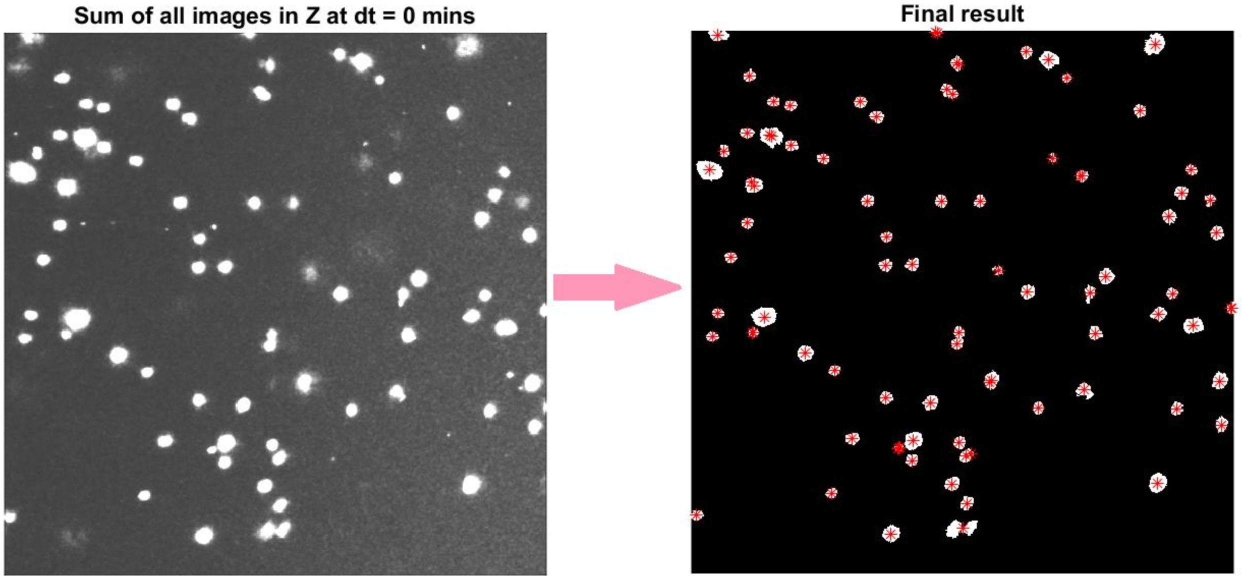

Figure 6.7. A visual representation of finding the cell centers from a Z-stack tensor. Here, to create an easier visualization, we have added all the Z-stack images at dt = 0 together to create a 2D view for the reader.

6.3.3. Cell Tracking Algorithm

The detected cell centroids from the previous step were used in Kalman filtering algorithm to track each cell over time (*73, 75, 77, 89, 90*). The Kalman filtering algorithm uses information from the past to predict the position of the cells in the next frame. The algorithm consists of two step processes: the first step predicts the location of the cells, and the second step uses the detected centroids to adjust the error in estimation of the cell location (*75, 76, 90*). As some cells leave and some enter the field of view during the imaging time, the algorithm keeps updating the tracks. If a cell is not found for four or more consecutive frames, the algorithm deletes its track assuming that the cell has left the field of view. After all the tracks are assigned, Kalman filter gives new labels to the unassigned detected centers assuming they have just entered the field of view.

One of the parameters used in this method is the cost of forcing the algorithm to keep assigning the cell number over time. If this parameter is increased the rate of losing a cell increases but at the same time, if this number is lowered, then the rate of error in tracking increases. As a result, a balance between the two scenarios is required. In our dataset as we had many cells in the field of view where some kept leaving, entering, or disappearing for a few minutes, we increased the cost. This was done because the purpose of our study was just looking at the total movements not just a specific cell movement.

As each experiment consists of 2000 images (40 frames and 50 Z-slice in each frame), each frame had more than 100 cells in it, labeling the cells manually was impossible. Therefore, calculating the exact accuracy rate of Kalman filtering algorithm was not feasible. As a result, we selected 40 random cells in one of the 10 nM fMLP experiments (as 10 nM fMLP experiments had the most active cells) and compared the assigned tracks manually. The results showed that the algorithm was able to correctly track the cells 92% of the time.

6.3.4. Cell Movement Classification

Similar to other studies, we witnessed three types of movements in our cell migration experiments:

- **Inactive**: Cells that stayed stationary at their place during the time of microscopy. A cell was labeled as inactive if its total movement in the XY plane was less than a pixel. The total amount of displacement in the Z coordinate was excluded in the calculations because we had small drifts in the Z direction while performing the experiments.
- **Lazy**: Cells that moved less than a predefined threshold during the experiments.
- **Active**: Cells that were our interest in analyzing their motility features as a function of chemoattractant concentration. These cells were divided into two subcategories: chemotaxis (showing a general directed movement toward the chemoattractant source) and chemokinesis (performing random movements inside the collagen).

To separate the active cells from the lazy ones, we first adjusted the Z-drifts in all the detected cell centers to minimize the error in our later calculations. As inactive cells stayed stationary in their place and as collagen was colorless under the confocal microscopy, they became the best and only candidates to find the amount of drift at each time point. Hence, for each time point, we calculated the average displacement of inactive cells from t_i to t_{i+1} and subtracted the result from all the centers at time t_{i+1}. The below figure represents the results before and after adjusting the centers in the inactive cells.

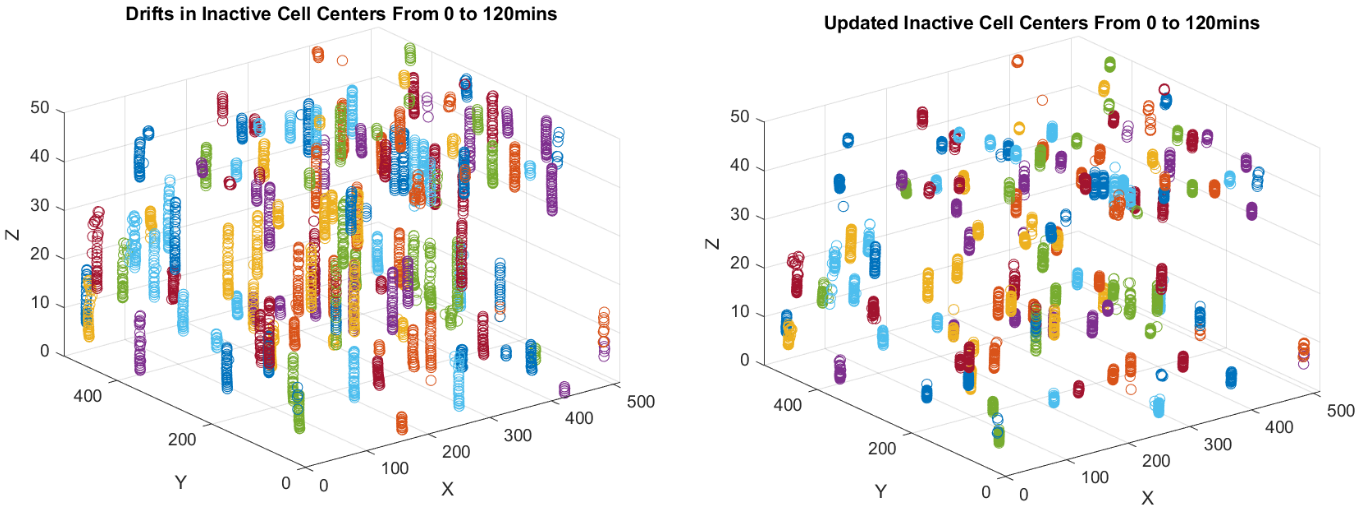

Drifts in Inactive Cell Centers From 0 to 120mins

Updated Inactive Cell Centers From 0 to 120mins

Figure 6.8. An example of drifts in inactive cells in the Z-direction and their adjusted centers. Each color represents a tracked cell center over time. As it is shown on the left figure, the cells are shifting down as time passes by. We adjusted the drifts in all the tracked cells to minimize the error in our calculations cells displacements and velocities in our later calculations.

After correcting the Z-drifts in all the cell centers, the below steps were taken to label the rest of the cells:

1. Each cell displacement excluding the inactive ones for all the experiments: Control, 10, and 100 nM fMLP, were calculated.
2. The lowest 25% quantile displacement in 10 nM fMLP experiments (that had the highest activity level) was calculated and set as the global threshold.
3. The cells with a higher movement above the threshold were labeled as active and the ones with a lower total displacement as lazy.
4. The active cells were then divided to two subcategories:

a. An active cell was labeled as chemotaxis if its total movement toward the source was higher than the absolute value of total movement in the Y and Z directions: $\sum_{t=i}^{k-1}(x_{t+1} - x_t) > \max(|\sum_{t=i}^{k-1}(y_{t+1} - y_t)|, |\sum_{t=i}^{k-1}(z_{t+1} - z_t)|)$, assuming the cell was seen from time *i* to *k*.

b. If the above condition was not met, the cell was labeled as chemokinesis (performing random movement).

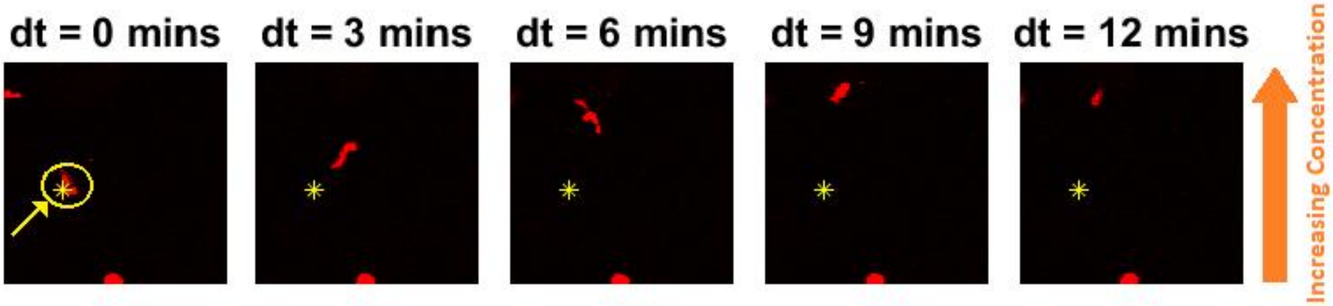

Figure 6.9. An example of a cell moving toward the fMLP source inside the collagen matrix.

6.4. Results

6.4.1. Cell Motility as a Function of Initial Chemoattractant Concentration

We compared the percentage of cells that belonged to active, chemotaxis, or chemokinesis groups in experiments with various initial concentrations (0, 10, and 100 nM fMLP). The results showed that the cell motility in 10 nM fMLP was the highest among control, 10 and 100 nM fMLP experiments (Figure 6.10). In addition, cells showed both more chemotaxis and chemokinesis behavior when the initial concentration of fMLP was 10 nM.

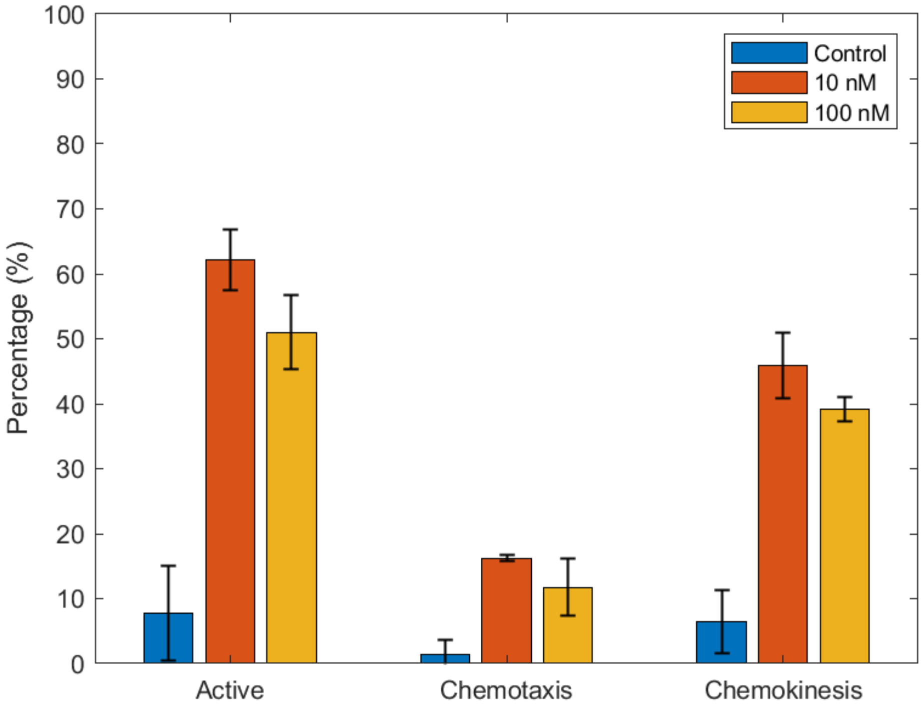

Figure 6.10. The percentage of cell activity state in different fMLP concentrations (0, 10, and 100 nM).

fMLP Concentration	**Total**	**Inactive**	**Lazy**	**Active**	**Chemotaxis**	**Chemokinesis**
Control	596	389 (**65%**)	145 (**24%**)	62 (**10%**)	13 (**2%**)	49 (**8%**)
10 nM	1263	297 (**23%**)	184 (**15%**)	782 (**62%**)	206 (**16%**)	576 (**46%**)
100 nM	788	254 (**32%**)	131 (**17%**)	403 (**51%**)	93 (**12%**)	310 (**39%**)

Table 6.1. This table represents the total number of the tracked cells in n = 3 experiments for each initial fMLP concentration. The highest percentage (in green) of cell motility was in 10 nM fMLP, and the lowest percentage (in red) of activity was observed in control experiments.

We performed a statistical significance test to determine the association between the concentration of chemoattractant (0, 10, 100 nM) and the activity state of cells (inactive, lazy, and active). Since the two variables in this test (concentration and activity state) are categorical, we performed the chi-square test (r × c contingency table) to assess the statistical significance. The test showed that the activity state of the cell is statistically significantly dependent on the concentration of chemoattractant ($p < 0.001$).

In addition, we performed the chi-square test to evaluate the association between the concentration of chemoattractant (10, 100 nM) and the proportion of migration behavior of active cells (chemotaxis vs chemokinesis). We did not include the control cells (0 nM fMLP) in this test since the number of active cells in this category was very small (Table 6.1). The results showed that the migration behavior of cells (i.e., whether an active cell performs chemotaxis or chemokinesis) is not statistically significantly dependent on the concentration of chemoattractant ($p = 0.2201$).

Although the proportion of active cells that performed chemotaxis was not statistically significantly dependent on the concentration of fMLP, the results from Student's two sample one sided *t*-test showed that the average velocity in the X-axis (toward the chemoattractant source) in 10 nM fMLP was statistically significantly higher than 100 nM fMLP ($p < 0.001$) (Figure 6.11).

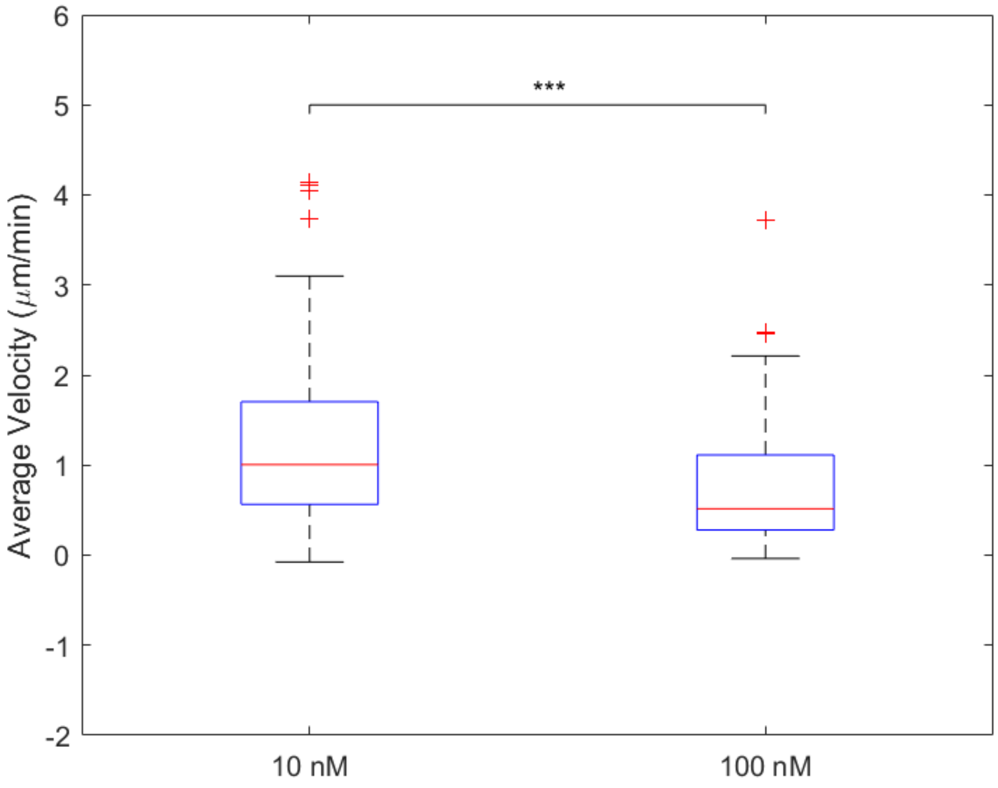

Figure 6.11. Average velocity toward the chemoattractant source (X-axis) in cells performing chemotaxis. The result from Student's two sample one sided *t*-test showed that the average velocity toward the chemoattractant source in 10 nM fMLP was statistically significantly higher than the 100 nM in the chemotaxis group ($p < 0.001$).

Additionally, we performed Student's two sample one sided *t*-test between the 10 and 100 nM fMLP in the chemokinesis group to check whether the average speed in 10 nM fMLP was also higher than 100 nM. Since chemokinesis involves movements in random directions, we focused on the cell speed rather than velocity in specific directions. The results showed that the average speed in 10 nM was statistically significantly higher than 100 nM fMLP in the chemokinesis group ($p < 0.001$) (Figure 6.12).

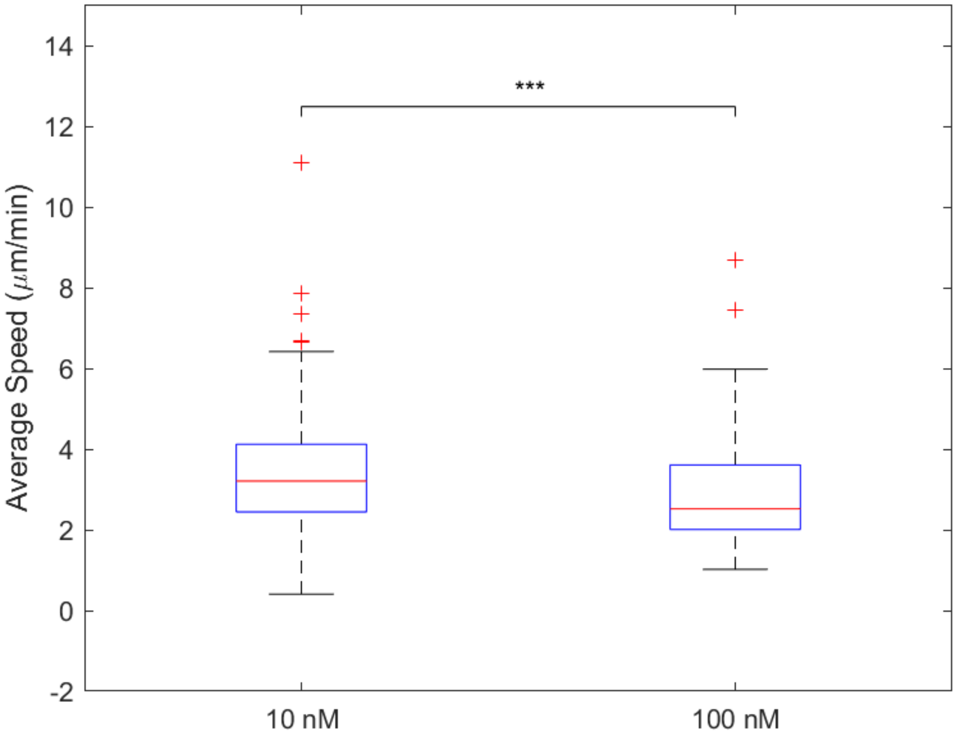

Figure 6.12. Average speed in cells performing chemokinesis. The result from Student's two sample one sided *t*-test showed that the average speed in 10 nM fMLP was statistically significantly higher than the 100 nM ($p < 0.001$).

6.4.2. Chemotaxis as a Function of Chemoattractant Concentration Gradient

As the cells were more active in 10 nM fMLP experiments, we selected the data from this group in the rest of the analysis. Since we calculated the fMLP diffusion coefficient using the dye experiments as discussed in Chapter 4. , we were able to calculate the concentration and concentration gradient of fMLP in the 3D collagen matrix at any location and time by solving the diffusion equation. This enabled us to estimate the concentration and its gradient at each cell’s location in every time frame, allowing studying the relationship between these quantities and cell motility.

In the chemotaxis group, we measured the correlation between cell velocities toward the source at any time point and the concentration gradient of the chemoattractant. As shown in Figure 6.13, understanding the correlation was difficult due to the large number and the wide distribution of data points . As a result, we discretized the X-coordinate to four equal sized bins and calculated the percentage of cells in each bin that showed movement in the positive X direction ($V_x > 0$). The results showed that this percentage increases up to a peak with the increase of concentration gradient and then decreases at very high concentration gradients, which means that the percentage of cells moving toward the source is highest at moderate concentration gradients (Figure 6.13).

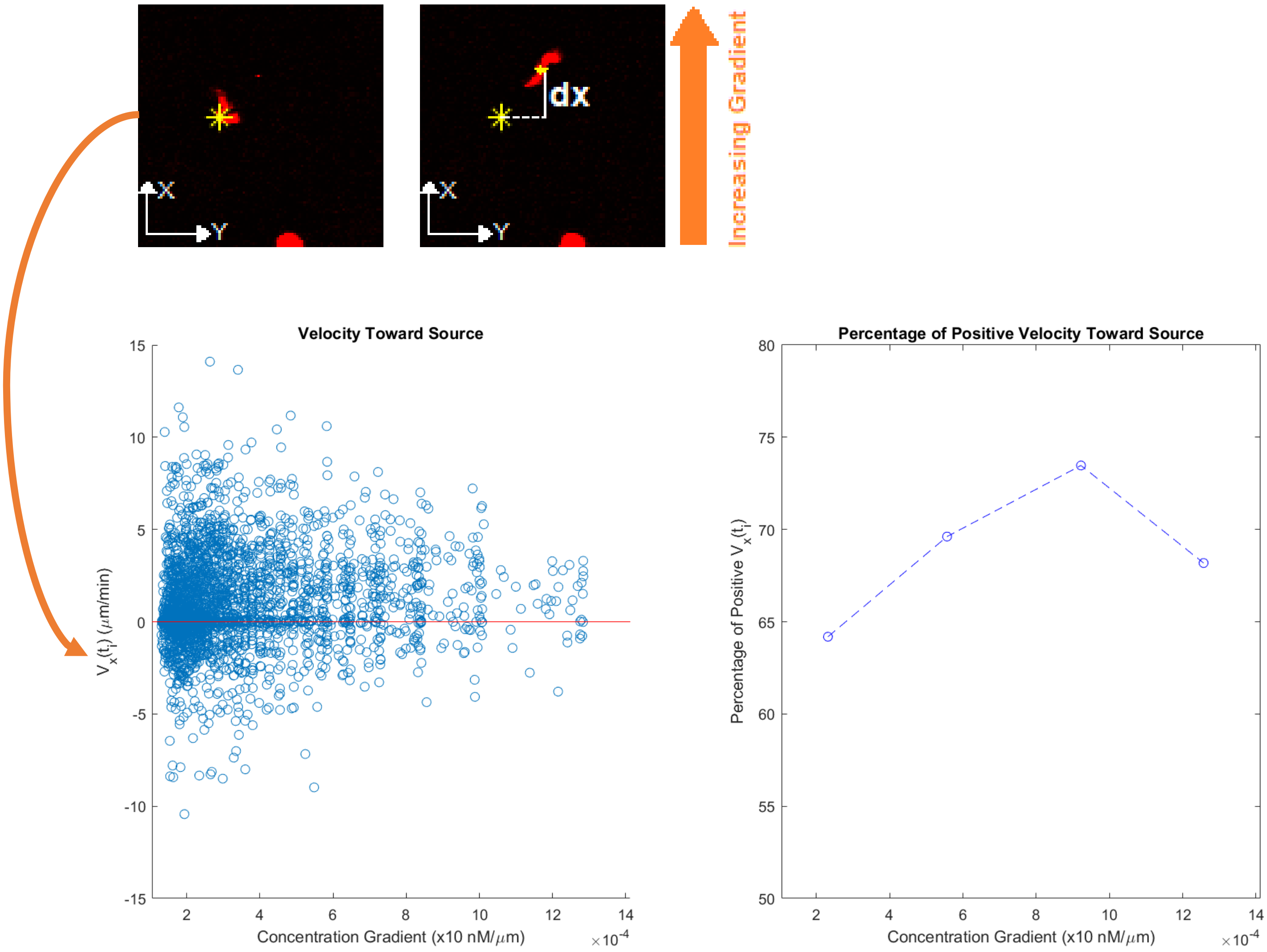

Figure 6.13. Velocity toward the source in the chemotaxis group. Each point on the left figure represents the velocity measurement in a single displacement from one time frame to the next frame where the cell was observed. The concentration gradient was discretized to four equal bins simplifying the pattern of velocities in the right figure. The percentage of positive velocities in each bin was calculated and plotted on the right figure.

Because the concentration gradient inside the collagen during the experiment was time-correlated, we did not know if the correlation patterns seen in Figure 6.13 were due to time or concentration gradient. Therefore, we improved our analysis by binning the data based on time to minimize the confounding effect of time on the correlation analysis. Figure 6.14 shows a heatmap of the percentage of cells with positive velocity toward the source where the two axes represent concentration gradient and time. Among all rows and columns in the heatmap, only the first row and first column contained data points in all bins. The results from the first column which excludes time as the confounding factor showed the same pattern seen in the 2D plot in Figure 6.13. Furthermore, the first row showed a steady decline in the percentage of positive velocities over time, indicating the effect of time on cell movements at that concentration gradient.

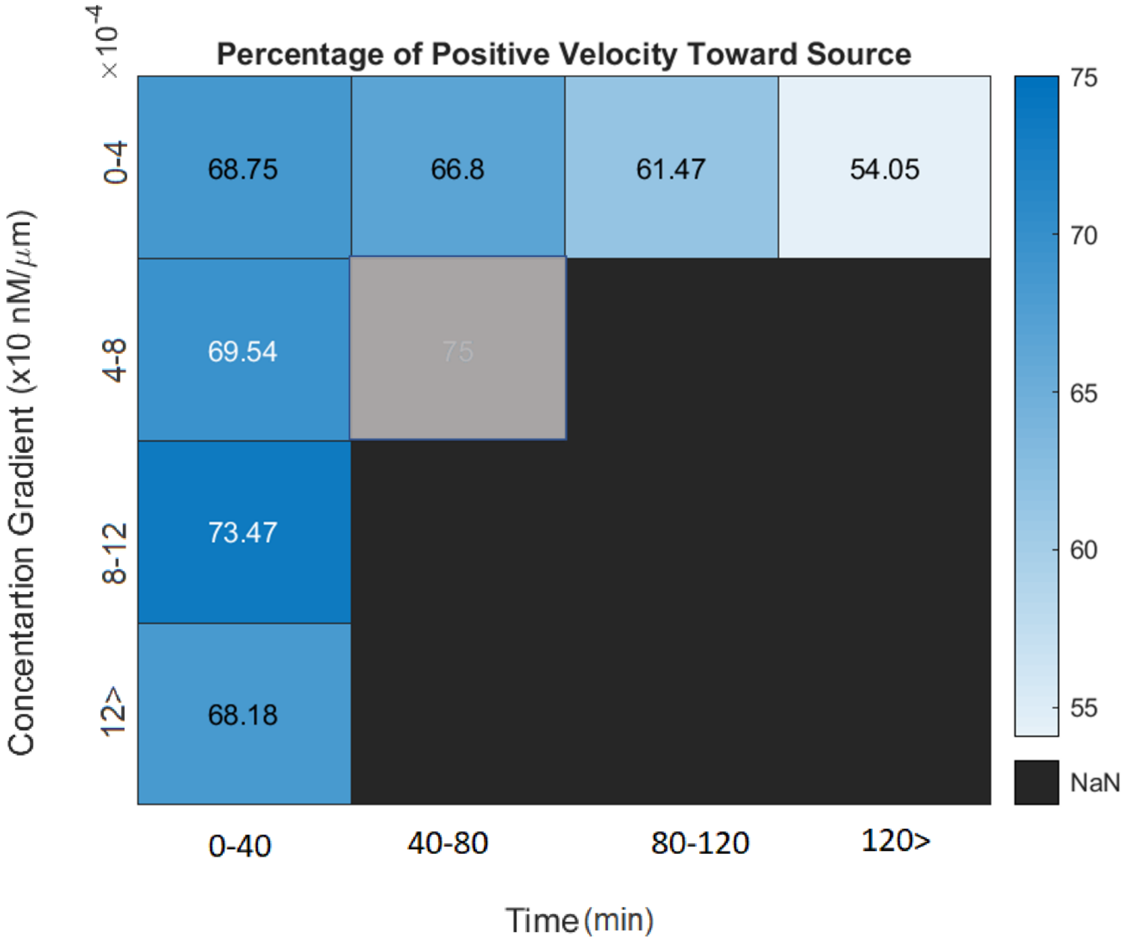

Figure 6.14. Heatmap of percentage of positive velocity toward source in chemotaxis. We binned the data based on time to minimize the confounding effect of time. The first column shows that the percentage of movements toward

the source is highest at moderate concentration gradients similar to Figure 6.13. In addition, the first row shows that the percentage decreases over time at low concentration gradients. Note: the bins containing less than 10 counts were grayed out and excluded from the analysis.

We also performed the same analysis for cell mean velocities in the X direction in the chemotaxis group (Figure 6.15 and Figure 6.16). Similar to the pattern of positive velocities, the results showed that average velocity was positively correlated with the concentration gradient in low to moderate gradient values.

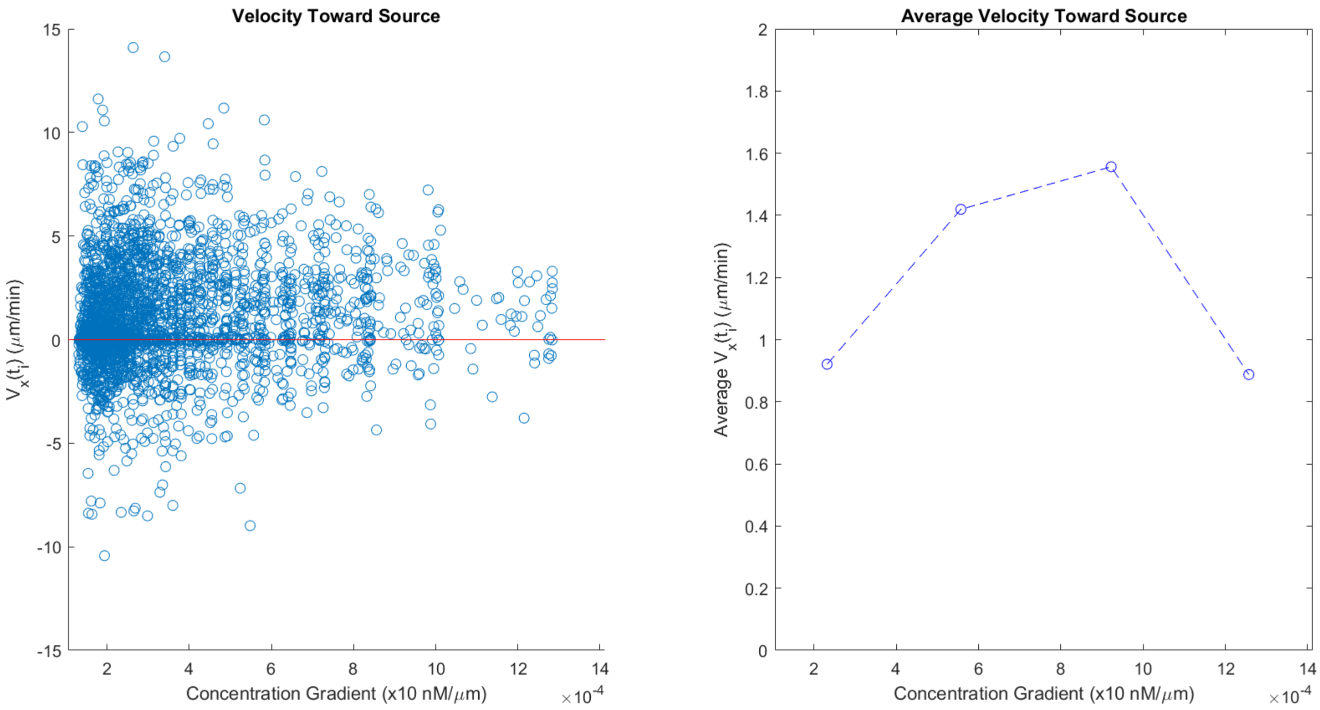

Figure 6.15. Average velocity in each concentration gradient interval in chemotaxis group. Each point on the left figure represents a velocity measurement in a single displacement from one time frame to the next frame where the

cell was observed. The concentration gradient was discretized to four equal bins simplifying the pattern of velocities in the right figure where the average velocity in each bin was plotted.

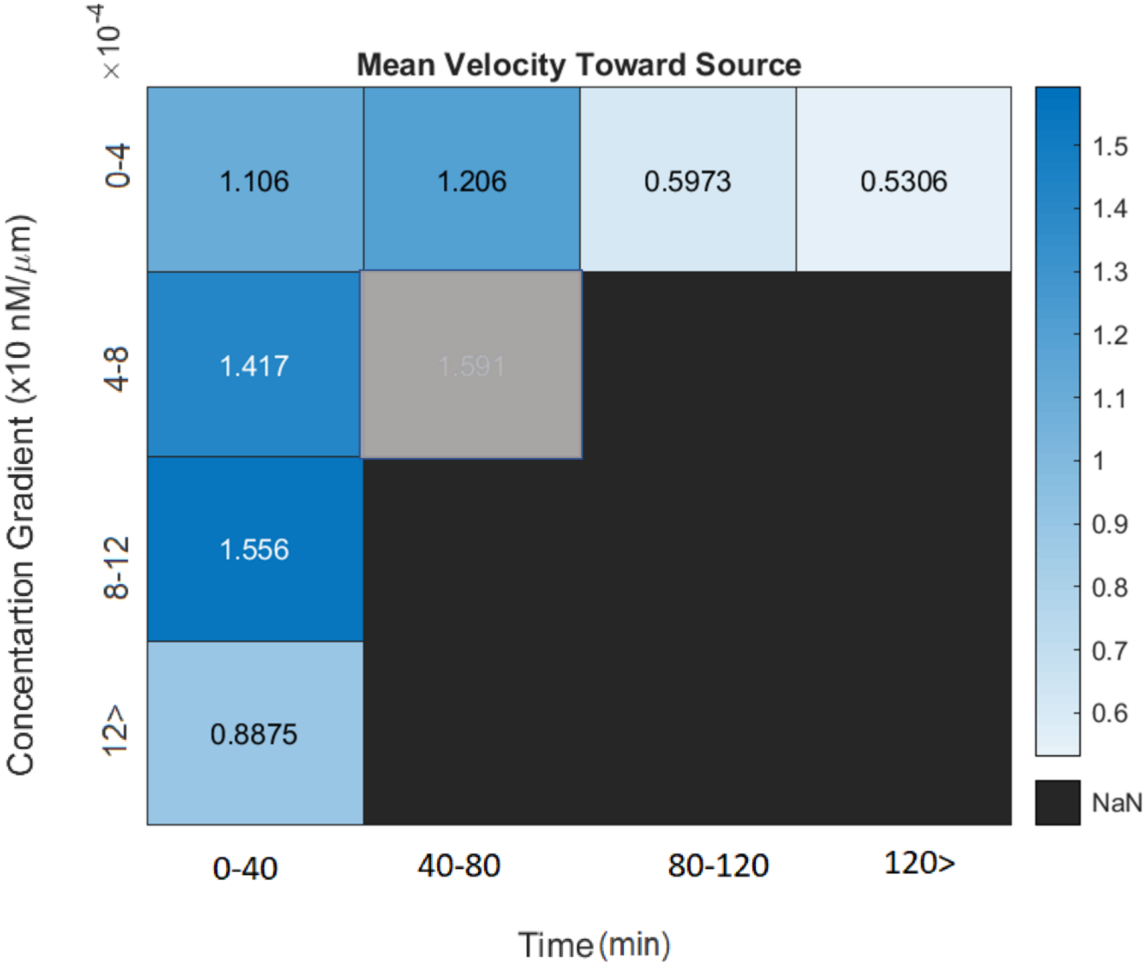

Figure 6.16. Heatmap of mean velocity toward source in chemotaxis. We binned the data based on time to minimize the confounding effect of time. The first column shows that the average velocity toward the source is highest at moderate concentration gradients similar to Figure 6.15. In addition, the first row shows that the velocity in cells has an overall decreasing pattern at later times. Note: the bins containing less than 10 counts were grayed out and excluded from the analysis.

6.4.3. Chemokinesis as a Function of Chemoattractant Concentration

Next, we analyzed the correlation between speed and fMLP concentration in the cells performing chemokinesis. Since chemokinesis involves movements in random directions, we focused on the cell speed rather than velocity in specific directions. We first investigated the dependence of average speed on chemoattractant concentration (Figure 6.17, left). Due to the large number and wide distribution of data points, we discretized the concentrations into four bins and calculated the average speed in each bin (Figure 6.17, right) which showed the highest speed occurring at moderate concentrations.

Because concentration inside the collagen during the experiment was time-correlated, we did not know if the correlation patterns seen in Figure 6.17 were due to time or concentration. Therefore, we improved our analysis by binning the data based on time to minimize the confounding effect of time on the correlation analysis. Figure 6.18 shows a heatmap of the average speed in cells where the two axes represent concentration and time. Among all rows and columns in the heatmap, only the first row and the second column contained data points in all bins. The results from the first column which excludes time as the confounding factor showed the same pattern seen in the 2D plot in Figure 6.17. In addition, the second row showed an overall decline in the average speed at later times within that concentration bin.

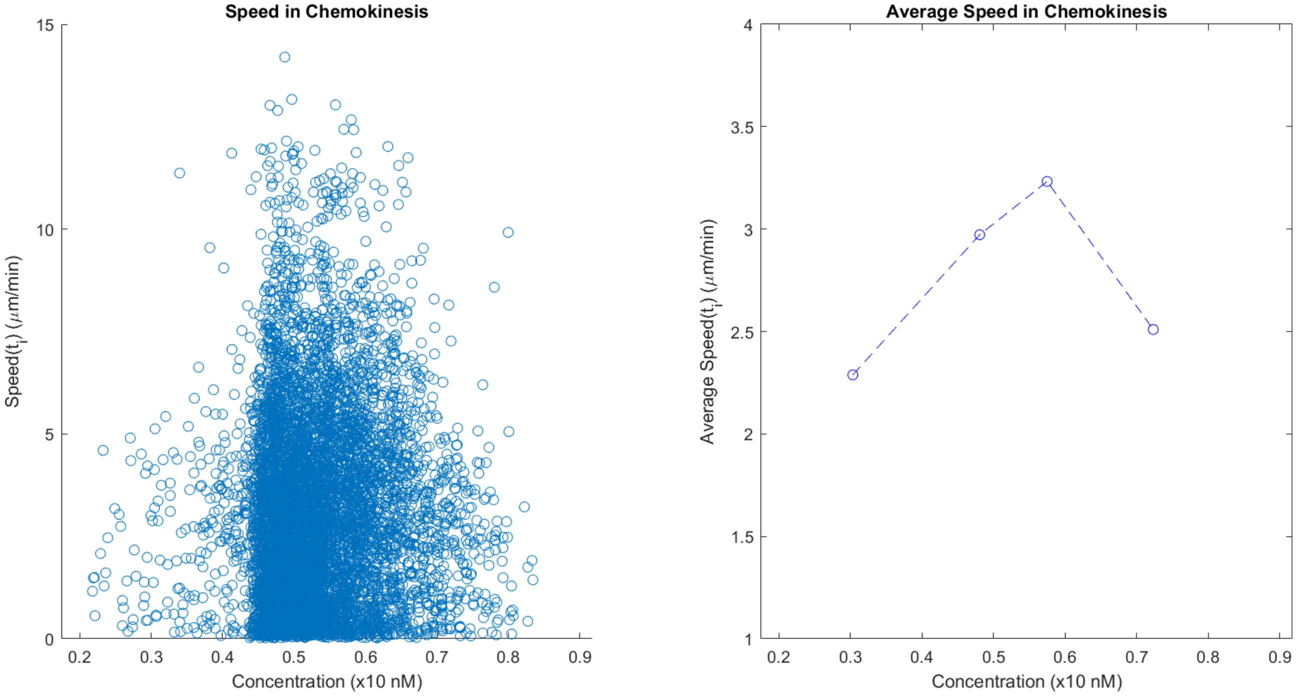

Figure 6.17. Speed as a function of chemoattractant concentration in chemokinesis group. Each point on the left figure represents the speed in a single displacement from one time frame to the next frame where the cell was observed. In the right figure, we discretized the concentration to four bins and calculated the average speed for each bin. The results showed that average speed was maximized at moderate concentration and was the lowest at very low or very high concentrations.

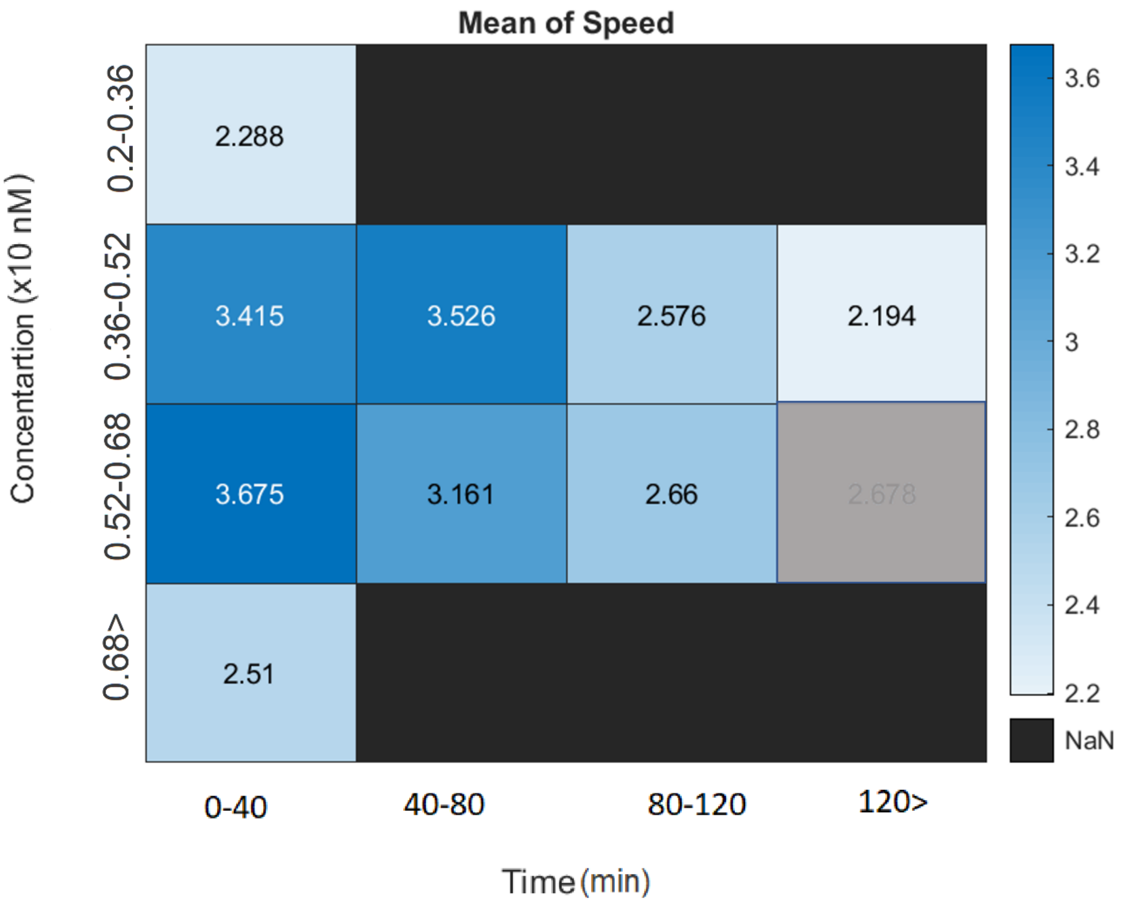

Figure 6.18. Heatmap of average speed in chemokinesis group. We binned the data based on time to minimize the confounding effect of time. The first column shows that the average speed is maximized at moderate concentrations when excluding the effect of time. In addition, rows two and three show that the average speed is the highest at earlier time points of the experiment within each concentration bin. Note: the bins containing less than 10 counts were grayed out and excluded from the analysis.

Chapter 7. Discussion

In this study we aimed to understand neutrophil-like cell migration behavior in the presence of a chemoattractant in an in-vitro environment. We designed an experimental setup to allow cell migration in a 3D environment composed of three compartments: chemoattractant source and sink on the sides and a collagen matrix with seeded cells in the middle compartment. To identify the pattern of cell migration as a function of chemoattractant concentration and time, we aimed to calculate the chemoattractant concentration and its gradient at any location and time inside the collagen, which required an estimate of the diffusion coefficient of our chemoattractant, fMLP, inside the collagen matrix. To achieve this, we investigated the diffusion of a fluorescent dye with a similar molecular weight as fMLP in our 3D system, measured its diffusion coefficient, and used it to solve the diffusion equation to quantify the chemoattractant concentration at any location and time.

To perform cell migration experiments, we used differentiated HL-60 (dHL-60) cells as an alternative of using primary neutrophils. Working with HL-60 cells is much simpler as they grow very quickly in-vitro with simple maintenance as opposed to short lived neutrophils that cannot be grown in-vitro. The cells were differentiated by adding DMSO to the cell-media for 6 days prior to performing the experiments. Using flow cytometry experiments, we showed that differentiating HL-60 cells upregulated the expression level of CD11b, the antigen that binds to fMLP. This result indicated that the selection of dHL-60 cells was an appropriate choice to study the cell migration in presence of fMLP.

After differentiation of HL-60 cells to neutrophil-like (dHL-60) cells, we examined how much fMLP was needed to be added to the source to maximize the percentage of cell activity in the experiments. Hence, we assessed cell experiments by adding three different initial fMLP concentrations (0, 10, and 100 nM) to the source and let it diffuse through the collagen with the seeded cells. We then automatically detected the cell centers and tracked the centers over time to calculate the total amount of displacement in each cell along each of the axes. Using the total amount of movements observed in each cell, we divided the cells into three different categories: inactive, lazy, and active. The percentage of active cells in each fMLP concentration (0, 10, and 100 nM) experiment was then calculated and compared, showing that the initial concentration of 10 nM fMLP at the source was optimal in creating cell motility.

Next, we separated the behavior of the active cells into two subcategories: chemotaxis (general directed movements toward the source) and chemokinesis (random movement in the collagen). We examined the total percentage of cells in each subcategory in the experiments (0, 10, and 100 nM fMLP) as well. 10 nM fMLP was again the winner in both of the subcategories representing that the experiments done in 10 nM concentration were the most suitable for studying both the chemotaxis and chemokinesis cell behaviors.

In addition to comparing the total number of cells in each category, we were interested to see whether the initial fMLP concentration also had an effect on the velocity and speed in chemotaxis and chemokinesis groups, respectively. The results from calculating Student's two sample one sided *t*-test showed that the average velocity in the X-axis (toward the chemoattractant source) in cells performing chemotaxis in 10 nM fMLP was statistically significantly higher than 100 nM fMLP ($p < 0.0001$). It is important to note that we excluded the control (0 nM fMLP) experiments in our analysis as the number of active cells in the control (0 nM) experiments was very low. We also analyzed the average speed in the cells performing chemokinesis in 10 and 100 nM fMLP using Student's two sample one sided *t*-test. The results demonstrated that average speed in 10 nM fMLP experiments were statistically significantly higher than 100 nM experiments. These findings indicated that releasing high amounts of chemoattractants from the source neither caused more cells to migrate nor caused the cells to migrate with a higher velocity or speed, implying that higher amounts of chemoattractant does not necessarily increase the cell motility. Moreover, based on the results, we concluded that the cell motility increases up to a point with the increase of fMLP concentration and then decreases at higher concentrations. This suggested that the peak of cell motility occurs below 100 nM fMLP. Thus, for future studies, we recommend choosing a concentration below 100 nM fMLP to obtain the highest cell motility in the environment.

As 10 nM fMLP experiments showed the most suitable environment for cell activity, we selected the data from this group to look at the pattern of cell motility as a function of chemoattractant concentration and its gradient over time. In the chemotaxis group, the correlation between the concentration gradient of the chemoattractant and the cell velocities toward the source showed that the cells expressed higher positive velocity in the X-axis (moving toward the source) at the moderate concentration gradients. The result showed that at very high concentration gradients, not only a lower percentage of cells exhibit positive velocity toward the source, but they show a lower average velocity as well. Next, in the chemokinesis group, we analyzed the correlation between the fMLP concentration and the cell speeds in the 3D environment. These results also showed that cell speeds were maximized at moderate chemoattractant concentrations. All of our results agreed with our previous conclusion that in general, moderate fMLP concentrations (e.g., 10 nM) can lead to a higher cell activity level than high concentrations (e.g., 100 nM).

Additionally, as the chemoattractant concentration during the experiments was time-correlated, we could not identify whether the decrease in cell activity at higher concentrations and its gradients were due to other underlying variables such as: the length of the experiments, or not having a supply of CO_2 during the experiments to maintain a balanced pH level in the collagen. Thus, to minimize the confounding effect of time on the analysis we binned the data based on time. The correlation analysis showed two different results:

1. In the same time bin, all the cell activity indicators were maximized at moderate fMLP concentrations and its gradient. This result was consistent with our previous analysis when we compared the cell activity indicator with fMLP concentration and its gradient across all times. From these analyses we concluded that, even after excluding the effect of time, the higher amounts of chemoattractant and its gradient have a negative effect on the migration of the cells and they reduce the velocity toward the chemoattractant source and speed in the chemotaxis and chemokinesis groups, respectively.
2. In the same concentration or its gradient bin, the results showed an overall decline in the average cell velocity in the chemotaxis and average cell speed in the chemokinesis groups. The exact reason for this finding is not clear. The decrease in cell activity indicators could have been due to the lack of CO_2 supply during the experiments, or simply because the cells were in a suboptimal in-vitro environment for a long period of time, causing the loss of cell motility over time.

In summary, although previous studies performed cell migration experiments and described the behavior of neutrophils or dHL60 cells in 1D or 2D assays in the presence of chemoattractants (*2, 30, 34, 35, 53*), their design limited the full 3D cell movements in-vitro. In our experimental setup, we allowed cells to move and change their shape in a three-dimensional space, possibly revealing results more relevant to the in-vivo cell behavior. In addition, our computational model not only automatically detected and tracked the cells in the 3D environment, but it allowed us to study the cell activity indicators with high spatiotemporal resolution of concentration and its gradient as well.

Chapter 8. Conclusion

Neutrophils, among all cells in the immune system, are the first to arrive at the site of infection to combat pathogens(*1-4*). In the presence of chemoattractants, these cells start a directed migration toward the damaged area. As they approach the injured area, they transmigrate to the tissue by squeezing in between endothelial cells and continuing migrating toward the higher chemoattractant concentrations to locate and destroy the invading pathogens. Therefore, understanding the neutrophil patterns of migration in presence of chemoattractants could ultimately lead to developing treatments for impaired immune cell diseases.

In this study, we aimed in understanding the patterns of neutrophil migration in the presence of N-Formyl-Met-Leu-Phe (fMLP) chemoattractant. But because neutrophils are short lived cells and they cannot be cultured in-vitro, we used HL-60 cells in our experiments. HL-60 cells grow in-vitro and double in suspension every few days and they can show similar activity behaviors as neutrophils when differentiated. In our research, by performing flow cytometry experiments we showed that treated HL-60 cells with DMSO make a proper alternative to study cell migration.

We designed a 3D chamber that contained three compartments creating a diffusion of fMLP from a side compartment to the middle compartment containing a collagen with seeded cells. Our experimental setup allowed us to create a concentration gradient in the environment to study the behavior of cells over time. In addition to creating 3D experimental setups, we designed a computational model that was able to automatically detect and track the cells in a 3D environment and predict the chemoattractant concentration and its gradient at any location and time. Both the experimental and computational designs allowed us to study the patterns of cell migration in a high spatiotemporal resolution of concentration and its gradient.

By analyzing our data, we divided the cells into inactive, lazy, and active cells and evaluated the association between the fMLP concentration (0, 10, 100 nM) and the cell activity state (inactive, lazy, and active). The results showed that the most suitable initial fMLP concentration for the active cells was 10 nM. At this concentration, not only the total number of active cells was maximized, but the cells also showed both the highest chemotaxis and chemokinesis behaviors. These results indicated that the initial concentration of 10 nM fMLP at the source was optimal in creating cell motility. In addition, further analysis of 10 nM fMLP experiments showed that as the fMLP concentration and its gradients increased up to moderate values (5 to 7 nM fMLP), the velocity in X-axis (toward the chemoattractant source) in the chemotaxis and speed in the chemokinesis groups also increased. However, at high amounts of chemoattractants, the velocity in X-axis in the chemotaxis and speed in the chemokinesis groups in the 3D environment decrease. This observation may perhaps point to the high amounts of chemoattractants present in the body as a possible cause of the inadequate neutrophil migration in severe sepsis. Furthermore, this suggests that levels of chemoattractants in the body might need to be moderated to have a beneficial impact in immune dysfunction diseases. Our results suggest that studying neutrophil migration as a function of chemoattractant concentrations could open a door to understand the neutrophil dysfunction in different diseases such as sepsis (*8, 9*), COPD (*22*-*25*), or severe COVID-19 (*26*-*28*) and therefore possibly contribute to designing treatments in the future.

Finally, we present possible improvements for future studies based on our learnings from our experiments:

- The size of the chemoattractant sink and the source could be increased to maintain their concentrations constant over time. This will remove the time dependency of the chemoattractant concentration profile and will significantly simplify the computational model.

- Because of the lack of CO_2 in our experimental setup, we could not determine the reason behind the decline of cell motility over time. Therefore, future studies could benefit from supplying CO_2 to the environment during the experiments and validating the cell motility with and without CO_2.
- Future studies could perform similar experiments with primary neutrophils and compare the results with dHL-60 cells. This could confirm that dHL-60 could serve as an appropriate model to study neutrophil migration.
- While applying the same computational model, future studies can modify our experimental model to investigate how cells behave in the presence of multiple chemoattractants in a 3D environment. For example, using multichannel pipettes, two chemoattractants can simultaneously be added to the two side compartments, diffusing through the collagen matrix located in the middle compartment while cell movements are being captured and analyzed in the collagen.

Bibliography

1. S. De Oliveira, E. E. Rosowski, A. Huttenlocher, Neutrophil migration in infection and wound repair: going forward in reverse. *Nature Reviews Immunology* **16**, 378-391 (2016).
2. B. Petri, M.-J. Sanz, Neutrophil chemotaxis. *Cell and tissue research* **371**, 425-436 (2018).
3. W. M. Nauseef, N. Borregaard, Neutrophils at work. *Nature immunology* **15**, 602-611 (2014).
4. A. W. Segal, How neutrophils kill microbes. *Annu Rev Immunol* **23**, 197-223 (2005).
5. Y. V. Lerman, M. Kim, Neutrophil migration under normal and sepsis conditions. *Cardiovasc Hematol Disord Drug Targets* **15**, 19-28 (2015).
6. T. N. Mayadas, X. Cullere, C. A. Lowell, The multifaceted functions of neutrophils. *Annual Review of Pathology: Mechanisms of Disease* **9**, 181-218 (2014).
7. S. Schmidt, M. Moser, M. Sperandio, The molecular basis of leukocyte recruitment and its deficiencies. *Molecular immunology* **55**, 49-58 (2013).
8. J. C. Alves-Filho, A. de Freitas, F. Spiller, F. O. Souto, F. Q. Cunha, The role of neutrophils in severe sepsis. *Shock* **30**, 3-9 (2008).
9. M. A. Kovach, T. J. Standiford, The function of neutrophils in sepsis. *Current opinion in infectious diseases* **25**, 321-327 (2012).
10. P. H. Leliefeld, C. M. Wessels, L. P. Leenen, L. Koenderman, J. Pillay, The role of neutrophils in immune dysfunction during severe inflammation. *Critical care* **20**, 1-9 (2016).
11. X. F. Shen, K. Cao, J. p. Jiang, W. X. Guan, J. F. Du, Neutrophil dysregulation during sepsis: an overview and update. *Journal of cellular and molecular medicine* **21**, 1687-1697 (2017).
12. F. Zhang, A.-L. Liu, S. Gao, S. Ma, S.-B. Guo, Neutrophil dysfunction in sepsis. *Chinese medical journal* **129**, 2741-2744 (2016).
13. R. C. Reddy, T. J. Standiford, Effects of sepsis on neutrophil chemotaxis. *Current opinion in hematology* **17**, 18-24 (2010).
14. M. Cecconi, L. Evans, M. Levy, A. Rhodes, Sepsis and septic shock. *The Lancet* **392**, 75-87 (2018).
15. M. M. Levy, L. E. Evans, A. Rhodes, The surviving sepsis campaign bundle: 2018 update. *Intensive care medicine* **44**, 925-928 (2018).
16. R. C. Bone *et al.*, Definitions for sepsis and organ failure and guidelines for the use of innovative therapies in sepsis. *Chest* **101**, 1644-1655 (1992).
17. J.-L. Vincent, S. M. Opal, J. C. Marshall, K. J. Tracey, Sepsis definitions: time for change. *Lancet (London, England)* **381**, 774 (2013).
18. C. L. Sprung *et al.*, An evaluation of systemic inflammatory response syndrome signs in the Sepsis Occurrence In Acutely Ill Patients (SOAP) study. *Intensive care medicine* **32**, 421-427 (2006).
19. C. N. Jones *et al.*, Spontaneous neutrophil migration patterns during sepsis after major burns. *PloS one* **9**, e114509 (2014).
20. L. Evans *et al.*, Surviving sepsis campaign: international guidelines for management of sepsis and septic shock 2021. *Intensive care medicine* **47**, 1181-1247 (2021).
21. C. Nathan, Neutrophils and immunity: challenges and opportunities. *Nature reviews immunology* **6**, 173-182 (2006).
22. S.-D. Lee, *COPD: heterogeneity and personalized treatment*. (Springer, 2017).
23. K. Hoenderdos, A. Condliffe, The neutrophil in chronic obstructive pulmonary disease. Too little, too late or too much, too soon? *American journal of respiratory cell and molecular biology* **48**, 531-539 (2013).
24. K. Blidberg, L. Palmberg, B. Dahlen, A. S. LANTZ, K. Larsson, Increased neutrophil migration in smokers with or without chronic obstructive pulmonary disease. *Respirology* **17**, 854-860 (2012).

25. C. Wang *et al.*, Progress in the mechanism and targeted drug therapy for COPD. *Signal transduction and targeted therapy* **5**, 1-20 (2020).
26. K. B. Belchamber *et al.*, Dysregulated neutrophil phenotype and function in hospitalised non-ICU COVID-19 pneumonia. *Cells* **11**, 2901 (2022).
27. M. Laforge *et al.*, Tissue damage from neutrophil-induced oxidative stress in COVID-19. *Nature Reviews Immunology* **20**, 515-516 (2020).
28. N. Reusch *et al.*, Neutrophils in COVID-19. *Frontiers in immunology*, 952 (2021).
29. A. Millius, O. D. Weiner, in *Chemotaxis*. (Springer, 2009), pp. 167-177.
30. K. A. Babatunde *et al.*, Chemotaxis and swarming in differentiated HL-60 neutrophil-like cells. *Scientific reports* **11**, 1-13 (2021).
31. S. O. Carrigan, A. L. Weppler, A. C. Issekutz, A. W. Stadnyk, Neutrophil differentiated HL-60 cells model Mac-1 (CD11b/CD18)-independent neutrophil transepithelial migration. *Immunology* **115**, 108-117 (2005).
32. S. K. Yadav *et al.*, Chemokine-triggered microtubule polymerization promotes neutrophil chemotaxis and invasion but not transendothelial migration. *Journal of leukocyte biology* **105**, 755-766 (2019).
33. R. M. Garner *et al.*, Neutrophil-like HL-60 cells expressing only GFP-tagged β-actin exhibit nearly normal motility. *Cytoskeleton* **77**, 181-196 (2020).
34. A. B. Hauert, S. Martinelli, C. Marone, V. Niggli, Differentiated HL-60 cells are a valid model system for the analysis of human neutrophil migration and chemotaxis. *The international journal of biochemistry & cell biology* **34**, 838-854 (2002).
35. M. Hattenkofer *et al.*, Time course of chemotaxis and chemokinesis of neutrophils following stimulation with IL-8 or FMLP. *European Journal of Inflammation* **16**, 2058739218819171 (2018).
36. K. I. Hulkower, R. L. Herber, Cell migration and invasion assays as tools for drug discovery. *Pharmaceutics* **3**, 107-124 (2011).
37. D. A. Stout, J. Toyjanova, C. Franck, Planar gradient diffusion system to investigate chemotaxis in a 3D collagen matrix. *JoVE (Journal of Visualized Experiments)*, e52948 (2015).
38. D. A. Stout *et al.*, Mean deformation metrics for quantifying 3D cell–matrix interactions without requiring information about matrix material properties. *Proceedings of the National Academy of Sciences* **113**, 2898-2903 (2016).
39. D. Irimia, Microfluidic technologies for temporal perturbations of chemotaxis. *Annual review of biomedical engineering* **12**, 259-284 (2010).
40. P. Lacy, Mechanisms of degranulation in neutrophils. *Allergy, Asthma & Clinical Immunology* **2**, 1-11 (2006).
41. M. Beyrau, J. V. Bodkin, S. Nourshargh, Neutrophil heterogeneity in health and disease: a revitalized avenue in inflammation and immunity. *Open biology* **2**, 120134 (2012).
42. L. E. Hind, W. J. Vincent, A. Huttenlocher, Leading from the back: the role of the uropod in neutrophil polarization and migration. *Developmental cell* **38**, 161-169 (2016).
43. M. Eisenbach *et al.*, *Chemotaxis*. (World Scientific Publishing Company, 2004).
44. P. J. Van Haastert, P. N. Devreotes, Chemotaxis: signalling the way forward. *Nat Rev Mol Cell Biol* **5**, 626-634 (2004).
45. P. V. Afonso *et al.*, LTB4 is a signal-relay molecule during neutrophil chemotaxis. *Dev Cell* **22**, 1079-1091 (2012).
46. J. R. Mathias *et al.*, Resolution of inflammation by retrograde chemotaxis of neutrophils in transgenic zebrafish. *Journal of leukocyte biology* **80**, 1281-1288 (2006).
47. J. Hughes *et al.*, Neutrophil fate in experimental glomerular capillary injury in the rat. Emigration exceeds in situ clearance by apoptosis. *The American journal of pathology* **150**, 223 (1997).

48. S.-Y. Tan, W. Weninger, Neutrophil migration in inflammation: intercellular signal relay and crosstalk. *Current opinion in immunology* **44**, 34-42 (2017).
49. O. Soehnlein, L. Lindbom, Phagocyte partnership during the onset and resolution of inflammation. *Nat Rev Immunol* **10**, 427-439 (2010).
50. C. Akgul, D. A. Moulding, S. W. Edwards, Molecular control of neutrophil apoptosis. *FEBS Lett* **487**, 318-322 (2001).
51. A. Millius, O. D. Weiner, in *Live Cell Imaging*. (Springer, 2010), pp. 147-158.
52. A. C. Rowat *et al.*, Nuclear envelope composition determines the ability of neutrophil-type cells to passage through micron-scale constrictions. *Journal of Biological Chemistry* **288**, 8610-8618 (2013).
53. P. A. Nuzzi, M. A. Lokuta, A. Huttenlocher, in *Adhesion protein protocols*. (Springer, 2007), pp. 23-35.
54. S. J. Collins, A. Bodner, R. Ting, R. C. Gallo, Induction of morphological and functional differentiation of human promyelocytic leukemia cells (HL-60) by componuds which induce differentiation of murine leukemia cells. *Int J Cancer* **25**, 213-218 (1980).
55. S. J. Collins, The HL-60 promyelocytic leukemia cell line: proliferation, differentiation, and cellular oncogene expression. (1987).
56. S. Collins, F. Ruscetti, R. Gallagher, R. Gallo, Normal functional characteristics of cultured human promyelocytic leukemia cells (HL-60) after induction of differentiation by dimethylsulfoxide. *The Journal of experimental medicine* **149**, 969-974 (1979).
57. S. A. Fischkoff *et al.*, Eosinophilic differentiation of the human promyelocytic leukemia cell line, HL-60. *The Journal of experimental medicine* **160**, 179-196 (1984).
58. A. Marra, M. Horwitz, H. Shuman, The HL-60 model for the interaction of human macrophages with the Legionnaires' disease bacterium. *The Journal of Immunology* **144**, 2738-2744 (1990).
59. J. W. Chiao, W. F. Freitag, J. C. Steinmetz, M. Andreeff, Changes of cellular markers during differentiation of HL-60 promyelocytes to macrophages as induced by T lymphocyte conditioned medium. *Leukemia Research* **5**, 477-489 (1981).
60. G. Birnie, The HL60 cell line: a model system for studying human myeloid cell differentiation. *The British journal of cancer. Supplement* **9**, 41 (1988).
61. M. T. Drayson, R. H. Michell, J. Durham, G. Brown, Cell proliferation and CD11b expression are controlled independently during HL60 cell differentiation initiated by 1, 25α-dihydroxyvitamin D3 or all-trans-retinoic acid. *Experimental cell research* **266**, 126-134 (2001).
62. A. Mullick *et al.*, GeneExpression in HL60 Granulocytoids and Human PolymorphonuclearLeukocytes Exposed to Candidaalbicans. *Infection and immunity* **72**, 414-429 (2004).
63. M. G. Ormerod, P. R. Imrie, Flow cytometry. *Methods Mol Biol* **5**, 543-558 (1990).
64. M. G. Macey, *Flow cytometry*. (Springer, 2007).
65. A. Adan, G. Alizada, Y. Kiraz, Y. Baran, A. Nalbant, Flow cytometry: basic principles and applications. *Critical reviews in biotechnology* **37**, 163-176 (2017).
66. H. M. Shapiro, *Practical flow cytometry*. (John Wiley & Sons, 2005).
67. A. Nwaneshiudu *et al.*, Introduction to confocal microscopy. *Journal of Investigative Dermatology* **132**, 1-5 (2012).
68. D. Semwogerere, E. R. Weeks, Confocal microscopy. *Encyclopedia of biomaterials and biomedical engineering* **23**, 1-10 (2005).
69. J. Pawley, *Handbook of biological confocal microscopy*. (Springer Science & Business Media, 2006), vol. 236.
70. S. Singer, J. Nelder, Nelder-mead algorithm. *Scholarpedia* **4**, 2928 (2009).

71. J. C. Lagarias, J. A. Reeds, M. H. Wright, P. E. Wright, Convergence properties of the Nelder--Mead simplex method in low dimensions. *SIAM Journal on optimization* **9**, 112-147 (1998).
72. F. Gao, L. Han, Implementing the Nelder-Mead simplex algorithm with adaptive parameters. *Computational Optimization and Applications* **51**, 259-277 (2012).
73. Q. Li, R. Li, K. Ji, W. Dai, in *2015 8th International Conference on Intelligent Networks and Intelligent Systems (ICINIS)*. (IEEE, 2015), pp. 74-77.
74. N. H. Ali, G. M. Hassan, Kalman filter tracking. *International Journal of Computer Applications* **89**, (2014).
75. J.-M. Jeong, T.-S. Yoon, J.-B. Park, in *2014 Proceedings of the SICE Annual Conference (SICE)*. (IEEE, 2014), pp. 941-946.
76. X. Li, K. Wang, W. Wang, Y. Li, in *The 2010 IEEE international conference on information and automation*. (IEEE, 2010), pp. 1862-1866.
77. H. A. Patel, D. G. Thakore, Moving object tracking using kalman filter. *International Journal of Computer Science and Mobile Computing* **2**, 326-332 (2013).
78. R. Szeliski, *Computer vision: algorithms and applications*. (Springer Science & Business Media, 2010).
79. C. Sha, J. Hou, H. Cui, A robust 2D Otsu’s thresholding method in image segmentation. *Journal of Visual Communication and Image Representation* **41**, 339-351 (2016).
80. S. L. Bangare, A. Dubal, P. S. Bangare, S. Patil, Reviewing Otsu’s method for image thresholding. *International Journal of Applied Engineering Research* **10**, 21777-21783 (2015).
81. R. F. Moghaddam, M. Cheriet, AdOtsu: An adaptive and parameterless generalization of Otsu's method for document image binarization. *Pattern Recognition* **45**, 2419-2431 (2012).
82. N. Otsu, A threshold selection method from gray-level histograms. *IEEE transactions on systems, man, and cybernetics* **9**, 62-66 (1979).
83. P. Soille, *Morphological image analysis: principles and applications*. (Springer Science & Business Media, 2013).
84. W. S. Cleveland, Robust locally weighted regression and smoothing scatterplots. *Journal of the American statistical association* **74**, 829-836 (1979).
85. W. S. Cleveland, LOWESS: A program for smoothing scatterplots by robust locally weighted regression. *American Statistician* **35**, 54 (1981).
86. S. Dubben, A. Hönscheid, K. Winkler, L. Rink, H. Haase, Cellular zinc homeostasis is a regulator in monocyte differentiation of HL-60 cells by 1α, 25-dihydroxyvitamin D3. *Journal of leukocyte biology* **87**, 833-844 (2010).
87. K. Nouri, R. Yazdanparast, Proliferation inhibition, cell cycle arrest and apoptosis induced in HL-60 cells by a natural diterpene ester from Daphne mucronata. *Daru: Journal of Faculty of Pharmacy, Tehran University of Medical Sciences* **19**, 145 (2011).
88. M. Fabbrini *et al.*, A new flow-cytometry-based opsonophagocytosis assay for the rapid measurement of functional antibody levels against Group B Streptococcus. *Journal of immunological methods* **378**, 11-19 (2012).
89. W. Luo *et al.*, Multiple object tracking: A literature review. *Artificial Intelligence* **293**, 103448 (2021).
90. J. Durbin, S. J. Koopman, *Time series analysis by state space methods*. (OUP Oxford, 2012), vol. 38.